

Bi-Shell Valve for Fast Actuation of Soft Pneumatic Actuators via Shell Snapping Interaction

Chuan Qiao, Lu Liu, and Damiano Pasini*

Rapid motion in soft pneumatic robots is typically achieved through actuators that either use a fast volume input generated from pressure control, employ an integrated power source, such as chemical explosions, or are designed to embed elastic instabilities in the body of the robot. This paper presents a bi-shell valve that can fast actuate soft actuators neither relying on the fast volume input provided by pressure control strategies nor requiring modifications to the architecture of the actuator. The bi-shell valve consists of a spherical cap and an imperfect shell with a geometrically tuned defect that enables shell snapping interaction to convert a slowly dispensed volume input into a fast volume output. This function is beyond those of current valves capable to perform fluidic flow regulation. Validated through experiments, the analysis unveils that the spherical cap sets the threshold of the snapping pressure along with the upper bounds of volume and energy output, while the imperfect shell interacts with the cap to store and deliver the desired output for rapid actuation. Geometry variations of the bi-shell valve are provided to show that the concept is versatile. A final demonstration shows that the soft valve can quickly actuate a striker.

1. Introduction

Pneumatic soft robotics is a rapidly evolving field of research that promises to expand the scope of current robotic applications. Distinct from classical rigid body robots, their pneumatic soft counterparts are typically fabricated from soft materials, e.g., elastomers,^[1,2] that can undergo large deformations to accomplish complex tasks. A diverse range of input sources are typically used to drive their motion; some resort to internal pressurized air,^[3–5] and others to external propellers, such as roller modules^[6] or moveable bodies.^[7] Functions that have been realized span a broad spectrum of motion, from locomotion, including galloping,^[8] swimming,^[9] crawling,^[10]

and climbing,^[11–13] to manipulation, such as gripping,^[14,15] stirring,^[16] and swallowing.^[7] An advantage offered by soft robots is that their elastic modulus is similar to that of soft biological tissues, imparting in them the ability to easily adapt to the local profile of adjacent objects, and making them suitable for applications that involve delicate interactions with humans,^[17,18] the handling of fragile objects^[14] and the adaptation to unknown environments.^[5] Pneumatic soft robots do not always require a complex control system of actuators, sensors and control algorithms, as rigid body robots typically do; rather their working principle is to achieve control mainly in a passive way, through either the tuning of the robot body compliance^[1,19,20] or the integration of a complex internal fluidic circuit.^[21–24] Others of their advantages include low mass and cost, high cycle life, availability at small length scales, and damage resistance to impact.^[2,25–27]

Key to actuating fluidic soft robots is to have an effective strategy that can power motion and enable complex movements. The most widely used method is pressure control, applied successfully to trigger motion of soft robots of various size.^[4,26,28] With this strategy, actuation can be rapid and inflation can occur at high speed through the delivery of high pressure^[4,15] low viscosity air, and/or by further optimizing the actuator design with the outcome of reducing the amount of air required for actuation.^[26] While effective, pressure-controlled actuation has a twofold drawback. First, for pressure generation and control, it requires a bulky pneumatic system that typically includes a pressure supply (e.g., air pumps or compressed gas tanks) and a set of hard valves (e.g., pressure regulators and solenoid valves). Second, fine control over the change in volume is difficult to achieve. For a soft robot, this might pose a problem. If motion is driven by the emergence of unstable events, the soft robot might lose its capacity to function properly. For example, a spherical cap embedded into a soft robot that is driven by external pressure will snap from the initial to its fully everted configuration, leaving no chance to access any intermediate states of deformation;^[29] if motion requires operation at these states, the soft robot will inevitably fail to do so.

An alternative to pressure-controlled actuation is volume control. This strategy allows for direct adjustment of the volume change. For example, a syringe pump can be used to dispense a precise volume of a fluid into the soft robot, and its

C. Qiao, Dr. L. Liu, Prof. D. Pasini
Department of Mechanical Engineering
McGill University
Montreal, Quebec H3A 0C3, Canada
E-mail: damiano.pasini@mcgill.ca

 The ORCID identification number(s) for the author(s) of this article can be found under <https://doi.org/10.1002/adv.202100445>

© 2021 The Authors. Advanced Science published by Wiley-VCH GmbH. This is an open access article under the terms of the Creative Commons Attribution License, which permits use, distribution and reproduction in any medium, provided the original work is properly cited.

DOI: 10.1002/adv.202100445

pressure-volume response can be registered.^[29–33] Besides this advantage, controlling the output volume avoids any jumps in displacement that a pressure control strategy would impose upon snap-through buckling. Volume control strategies used so far, however, have a common drawback; they are unable to drive fast actuation, a limitation ascribed to the limited flow rate that a syringe pump can typically deliver. Only a handful of attempts have been successful to circumvent this issue, and all of them have been devoted to the design of actuators. Their strategy has been to integrate snap-through instability of spherical caps^[31] or balloons^[32] into the architecture of the actuator.

Besides pressure-controlled and volume-controlled actuation, other actuation methods used in the literature resort to external manipulation,^[6,7] dielectric elastomers,^[34–37] evaporation of low-boiling point fluids,^[38] chemical decomposition,^[23] and explosive chemical reaction.^[39–42] Their application to soft robots has so far shown to be limited due to the additional components they require, including external mechanisms for manipulation, electrical circuits for dielectric elastomers, heaters for low-boiling point fluids, and integrated systems for chemical decomposition and combustion.

Pneumatic soft robots typically resort to elements other than actuators to operate. One of them is valves. Their function so far has been other than that of actuators. Current valves can control the fluid flow spreading throughout the body of a soft robot. Some concepts comprise rigid elements that can provide a simple and unambiguous control of a fluid flow. Others achieve this function by engaging elastic instabilities, e.g., wrinkling, snapping, and creasing, in their constituents. Sources used to initiate elastic instabilities include air pressure supply, external force, and viscous flux through unstable-arch channels. In all cases, the fluid-control function these valves perform is binary, switching between two distinct states. For example, a spherical cap embedded in the valve has been shown effective to snap from one position to either block or unlock the flow in its internal tubes.^[29] Another valve architecture exploits the snapping of an elastic arch embedded in a fluid flow to act as a passive microfluidic fuse that regulates the flow present in its rigid-walled channels.^[43] Manifold applications exist for soft valves ranging from soft ring oscillators^[44] to pneumatic logic gates^[22] and soft kink valves.^[45] All the existing implementations can only either fully (on-off control) or partially (binary flux control) block a fluid flow for continuous operation, but cannot provide an impulse for fast actuation under volume control.

In this work, we introduce a bi-shell valve that can provide volume-controlled rapid actuation to soft actuators. The valve does not resort to the fast volume input typically generated through pressure control^[4,15] strategies, nor to any modifications to the body of the actuator that require chemical explosion^[39–42] or elastic instability.^[31,32,36,37] The valve engages snapping and shell interaction to generate a fast volume output upon a slow volume input. Our bi-shell valve can thus perform a function that is unattainable by existing soft valves. It has the following merits for soft robotics: i) Ready for use with volume control: Common soft actuators can directly use this valve to achieve rapid motion under volume control, without any additional modifications to the body of the actuator. ii) Output performance attuning: The amount of fast volume output can be set in a fully passive way by simply programming the geometry of the constituent shells and

their defects to maximize the valve performance and satisfy the functional requirements of a given soft robot. iii) Retainment of pre-snapping geometry: The volume output of the valve is negligible before snapping, thus enabling the soft actuator connected to our valve to preserve its initial undeformed state. iv) Inlet flow rate insensitivity: The fast volume output is not sensitive to the flow rate at the valve inlet, as the output is generated from the air transfer between the constituent shells during snapping. In the following sections, we first study the snapping and interaction between the elastic shells of our bi-shell valve to understand the role that each of them plays during deflation. We then characterize the response of each shell within a wide geometric space and map the range of fast volume outputs our bi-shell valve can achieve. Finally, we demonstrate the application of our bi-shell valve to thrust the motion of an object along a guided track.

2. Results and Discussion

2.1. The Bi-Shell Valve Concept: Tapping into Shell Snapping Interaction

Our bi-shell valve consists of two interacting elastic shells that cooperate upon snapping to generate a rapid change in volume in response to a slow volume input. **Figure 1A** shows the bi-shell valve concept in its undeformed state. Beneath the shells, an input chamber connecting the shell inner volumes provides deflation under volume control as well as pressure control, if required. On the left-hand side is a perfect spherical cap which exhibits an unstable response, typical of elastic thin shells with a high peak of pressure attained in the nearly undeformed state, followed in turn by a rapid fall of pressure into a plateau leading to full eversion.^[46] On the right-hand side is a hemispherical shell featuring a large axisymmetric imperfection in the form of an elliptical arc traced away from the pole. We select this imperfect shell for its stable response over a large change in volume that can be effectively tuned by the geometry of the imperfection, thus attaining a capacity to provide increasing pressure resistance.^[47] The bi-shell valve operates through a slow deflation (negative pressure) imparted by the inlet of the input chamber and delivers a fast deflation via the outlet at the output chamber. Since the pressure of the bi-shell valve remains negative during the operation, we have made here the assumption of neglecting the negative sign for the convenience of the analysis.

By combining the two shell architectures, a perfect spherical cap and an imperfect shell, each with its own distinct response, into one bi-shell system (**Figure 1A**), we can program the mechanism of deformation, impart a desired sequence of deflation, and code the global performance of our valve. Our goal is to capitalize on shell snapping interaction to generate a function that adds to the control-flow function of existing soft valves that would be otherwise unattainable through current concepts involving either snapping of a single spherical cap or other strategies.

We start with a description of the qualitative response of the system deformation. **Figure 1B** illustrates that a slow deflation of the input chamber through the inlet (ΔV_{in}), brings each shell into different states. At the onset of deflation (light green), the pole of the imperfect shell deforms downward smoothly without snapping from the initial state to state (i), whereas the perfect cap barely undergoes any deformation, hence retaining its initial

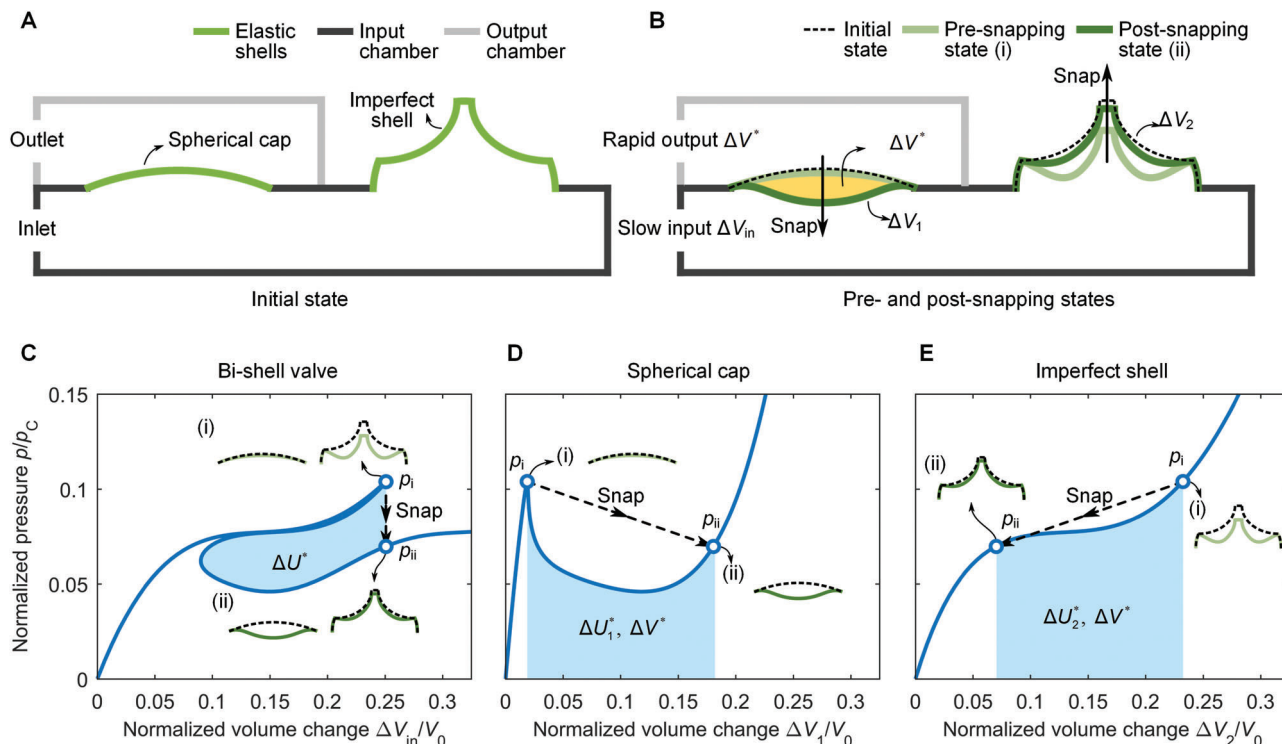


Figure 1. Bi-shell valve with snap-through response under volume control. A) Schematic of the bi-shell system in its unloaded state; the valve comprises two thin elastomeric shells, one with perfect and the other with imperfect spherical geometry, connected through an input chamber (below both) and output chamber (above the spherical cap). B) Pre and post snapping states of the bi-shell valve under incremental deflation ΔV_{in} . Prior to instability (light green) the spherical cap is almost locked in its initial shape yielding no change in volume ΔV_1 as opposed to its imperfect counterpart, which can deform downward smoothly without snapping from the initial state to state (i) and store elastic energy due to its compliance with an accrued change in volume ΔV_2 . There is no snapping during these stages because the instability is triggered by the buckling of the spherical cap. Upon snapping (dark green), the former bounces down to its buckled shape with a volume change of ΔV^* , whereas the latter springs up from state (i) to state (ii) with a release of ΔV^* . In yellow is the resulting ΔV^* , i.e., the volume difference between pre (i) and post (ii) snapping states, which describes the rapid change in volume generated by the snapping of the spherical cap. C–E) Pressure-volume responses of the entire bi-shell system (C), the spherical cap solely (D), and the imperfect shell only (E). The normalization factors of pressure and volume are the buckling pressure $P_C = 2E(t/R)^2/\sqrt{3(1-\nu^2)}$ and enclosed volume $V_0 = 2\pi R^3/3$ of a baseline hemispherical shell with radius identical to the radius R on the bottom plane of the constituent shells.

state (hidden line overlaid on light-green solid line). There is no snapping during these stages because snapping is triggered by the buckling of the spherical cap. After snapping (dark green), the imperfect shell springs back from state (i) to state (ii), whereas the spherical cap everts downward from its initial upward position.

To capture the snapping behavior in quantitative terms, we determine the pressure-volume response of the bi-shell valve. We first assess how the volume change of the input chamber governs the pressure of the input chamber, and then normalize these values respectively by the buckling pressure $P_C = 2E(t/R)^2/\sqrt{3(1-\nu^2)}$ and the enclosed volume $V_0 = 2\pi R^3/3$ of a baseline hemispherical shell with radius identical to the radius R on the bottom plane of the constituent shell. These metrics are the characteristic axes of the plot reported in Figure 1C. While deflation can be expected to generate negative values of both volume and pressure, here we consider their signs as positive for the convenience of the analysis. The portion of the curve up to (i) describes the initial deformation prior to snapping when the pressure hits the snapping pressure p_I . A further deflation triggers a snap-through instability with a configurational change in both shells, now reaching simultaneously their second state (ii) of equilibrium. The process is characterized by a drop of pressure to

p_{II} with the spherical cap eversion synchronous to the snap back of the imperfect shell. Since the outer side of the former shell is enclosed by the output chamber, its downward snapping produces a rapid change in volume (yellow area ΔV^* , Figure 1B), which is bounded by the pre- and post-snapping states of the spherical cap in the output chamber. The hallmark of this concept is that the release of volume to slow deflation is fast and would be otherwise inaccessible by employing either shell individually, as shown later. As per the energy and volume change in the input chamber, the snapping event causes a release of the previously stored elastic energy in both shells (ΔU^*) but with almost no change in volume (less than 0.54% of the total volume); this outcome is due to the extremely small difference in pressure (less than 550 Pa) between the input chamber and the atmosphere (see the Supporting Information for details).

2.2. Inferring the Bi-Shell Valve Behavior from the Individual Response of Each Shell

As described above, the deformation of our bi-shell system (Figure 1C) is the result of the collective response of the constituent

shells, each cooperating distinctly during deflation and snapping. To understand the interaction between them and each of their roles, here we examine each shell separately, investigate their individual responses when deflated separately, and correlate them to the system behavior.

Figure 1D pertains to the spherical cap on its own, and Figure 1E to the imperfect shell on its own. The former (blue path in Figure 1D) shows the characteristic highly unstable response of a perfect elastic shell. A small volume change ($\Delta V_1/V_0 < 0.02$) makes the pressure quickly escalate to a high critical value ($p/p_C = 0.104$, p_i), which immediately drops to a lower plateau ($p/p_C = 0.05$), spanning a wide range of volume change ($0.05 < \Delta V_1/V_0 < 0.2$). After the plateau, the pressure increases rapidly again. There is no limit point in volume because the spherical cap selected here is thick and shallow, similar to the findings of Gorissen et al.^[31]; the elements that are here important to trigger snapping are the initial peak in pressure, the subsequent softening, and a final increase in pressure as noted by Overvelde et al.^[32]. The latter shell of our valve exhibits a stable pressure response (blue path in Figure 1E) over an increasing volume change ΔV_2 , and its buckling mode is enabled by the size and location of the imperfection (see the Supporting Information for details). The pressure-volume path (blues) has three portions: an initial rapid increase of pressure for small values of the volume change ($\Delta V_2/V_0 < 0.1$), followed by a stable plateau offering a gradual increase of pressure for intermediate values of $\Delta V_2/V_0$, and finally a steep increase of pressure. While the blue paths in Figure 1C,D,E represent the static equilibrium responses of each system, the black hidden ones with arrow mark the direction from the pre to the post snapping state.

Once the individual shells join through the input chamber, a concerted deformation (Figure 1C) takes place to ensure equilibrium of volume and pressure. Equilibrium requires the balance of their pressure in the stable post-snapping state (see the Supporting Information). The conservation of volume requires the input volume change ΔV_{in} to equal the sum of the volume changes of the individual shells, ΔV_1 and ΔV_2 .^[32,33,48,49] The onset of snapping is mainly controlled by the spherical cap, which upon winning the critical pressure p_i , cannot accommodate any further increase in pressure, resulting in a sudden drop of pressure due to its elastic instability (Figure 1D). It is this event that triggers the snapping of both shells (black paths in Figure 1C,D,E). Each shell springs into its own snapped state in a swift manner. During snapping, the spherical cap collapses due to its reduced pressure resistance and propels the air in the input chamber toward the adjacent shell for an upward push; the sudden deflation of the former inflates the latter.

As with other forms of elastic deformation, during snapping each shell can store and release elastic energy (cyan areas in Figure 1), and their amounts correlate with those of the entire system. In particular, the deflation of the spherical cap by a volume change ΔV^* is accompanied by the storage of elastic energy ΔU_1^* (Figure 1D), while the inflation of the imperfect shell by a volume of ΔV^* corresponds to the elastic energy release ΔU_2^* (Figure 1E). The difference between them, $\Delta U^* = \Delta U_2^* - \Delta U_1^*$, is the elastic energy released by the bi-shell valve due to the snapping of both constituents (Figure 1C), a notion consistent with the existing literature.^[31–33,48,49] In addition, we note that the energy stored by both shells in the linear portion of the pressure-volume curves is

not considered here because it does not contribute to the energy output during snapping.

2.3. Experimental Investigation

Figure 2A shows our bi-shell valve fabricated with two thin shells (green) made out of Zhermack Elite Double 32 (Zhermack, Italy), along with acrylic input (painted in black) and output (transparent) chambers (see the Supporting Information for details). Figure 2B,C illustrates the mechanism of deformation at two sequential instants (pre and post snapping) upon deflation, with configurations that parallel those shown in Figure 1. In the imperfect shell, an axisymmetric mode of deformation first accrues until state (i) is reached, while the spherical cap holds its undeformed shape under initial pressure reduction (Figure 2B). Further deflation causes both shells to snap into distinct states (ii), the imperfect shell nearly springing upward to its initial configuration and the perfect shell buckling downward (Figure 2C and Movie S1; Supporting Information).

Figure 2D–F shows the pressure-volume change curves obtained from both our analyses and experiments (see the Supporting Information for details). The responses on all fronts, i.e., bi-shell valve, spherical cap, and imperfect shell, show a snapping behavior matching those in Figure 1C–E. In Figure 2D, the experimental pressure of the input chamber (blue curve) first increases smoothly upon air deflation until state (i) ($\Delta V_{in}/V_0 = 0.32$), and then plunges from $p_i/p_C = 0.128$ to $p_{ii}/p_C = 0.064$. Here, the experimental results confirm that the drop in pressure is triggered by the snapping of the spherical cap, which collapses downward (Figure 2C). The prediction of our numerical simulation (red curve) agrees with the experimental results, with the predicted pre- and post-snapping states (i) and (ii) resembling those of their experimental counterparts as quantified below.

While the volume change and energy output of the bi-shell valve cannot be directly calculated from the experimental curve (pressure-volume change) in Figure 2D, we can still estimate their values through the separate response of their elastic constituents, i.e., spherical cap and imperfect shell (blue curves in Figure 2E,F). The post-snapping pressure is determined through the equilibrium condition the two shells should satisfy at $p_{ii}/p_C = 0.062$ (Figure 2E,F), which is close to the value, $p_{ii}/p_C = 0.064$, from our experimental result in Figure 2D. The relative error between the estimated and measured post-snapping pressure is below 4%, demonstrating the accuracy of our estimation. From state (i) to state (ii), the volume change due to snapping is then obtained from the separate response of each shell as $\Delta V^*/V_0 = 0.154$, while the energy output is $\Delta U^*/(p_C V_0) = 3.57 \times 10^{-3}$. Our analysis provides an accurate prediction of the valve response, described by a volume change of $\Delta V^*/V_0 = 0.135$ and a released energy of $\Delta U^*/(p_C V_0) = 3.63 \times 10^{-3}$. To minimize the error between numerical and experimental results, we employ a realistic model that accounts for any non-uniformity of shell thickness caused by manufacturing as well as for the initial deformation due to clamping (see the Supporting Information for details). The discrepancy, especially at larger strains, is attributed to imperfections in shell geometry that emerge during fabrication. This might include geometric deviation of the mold from the nominal design, as well as defects in the base material, such as microvoids.

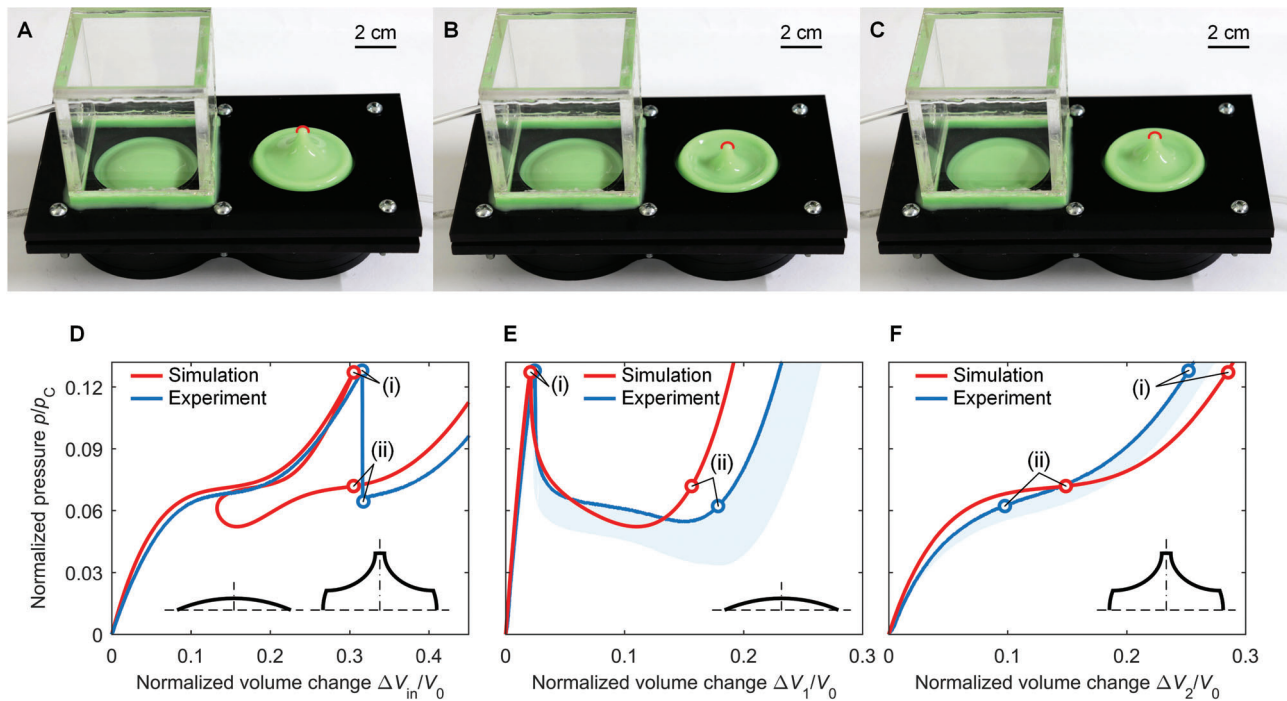


Figure 2. Experiment of the bi-shell valve. Photographs of bi-shell valve: A) initial state, B) state (i) before snapping, and C) state (ii) after snapping. The top of the imperfect shell is outlined with a red cap to emphasize the difference between states. D–F) Pressure-volume responses of the input chamber, the spherical shell, and the imperfect shell. P_C is the theoretical critical pressure of a perfect spherical shell and V_0 is the volume of a hemisphere. The cyan domains in (E) and (F) show the envelope of the experimental response of three tested samples.

The results from both analyses and experiments (Figures 1 and 2) reveal that shell interaction governs the bi-shell valve behavior, which in turn can be retrieved by combination of the individual shell response. These insights not only enable us to understand the role of each shell during snapping, but also provide principles for valve design involving multiple shells. We propose a two-steps approach (see Figure S16 for a flowchart of the design process in the Supporting Information), where the bi-shell performance is defined by 4 metrics: the upper bounds of volume and energy, $\Delta V_{\text{upper}}^*$ and $\Delta U_{\text{upper}}^*$, as well as the working ranges of ΔV^* and ΔU^* , i.e., the variation of volume change and released energy within their respective bounds. The first step involves examining the spherical cap only, which sets the valve performance limits, and aims at determining the upper bounds ($\Delta V_{\text{upper}}^*$ and $\Delta U_{\text{upper}}^*$) of the valve output. These bounds set the upper boundaries for the bi-shell valve performance, i.e., the bi-shell system with a given spherical cap cannot exceed them for any geometric scenario of the imperfect shell. In the second step, we determine the attainable ranges of volume change ΔV^* and released energy ΔU^* for the bi-shell by exploring the design space of the imperfect shell for a prescribed geometry of the spherical cap. With this approach, we can ensure that we reach the full potential of both shells, thereby yielding a valve output close to the achievable maximum.

2.4. Upper Bounds of Volume Change and Released Energy

The goal is to find the first two performance metrics of our bi-shell valve, i.e., the maximum values of volume change, $\Delta V_{\text{upper}}^*$,

and released energy, $\Delta U_{\text{upper}}^*$, our bi-shell valve can attain. As described earlier, the spherical cap sets the upper performance limit of our bi-shell valve, and is studied here as standalone shell. The modified Riks method is employed to simulate the deflation of a spherical cap subject to uniform pressure and parametrically map $\Delta V_{\text{upper}}^*$ and $\Delta U_{\text{upper}}^*$ upon snapping. The parameters defining the spherical cap geometry (inset in Figure 3) are the radius in the base plane ($R = 25\text{mm}$), the normalized thickness (varying between $t_1/R = 0.01$, and 0.1), and the normalized height (ranging from $h/R = 0.1$ to 0.5).

Figure 3A shows a representative curve of pressure versus volume change for a perfect spherical cap. The end point (light green) of the pre-snapping path denotes the pressure peak p_i (state (i)), which is typically above the end point of the post-snapping path (dark green designating state (ii)) at p_{ii} . As shown in Figure 1C–E, the drop of pressure from p_i to p_{ii} represents the reduction in pressure resistance offered by the imperfect shell. The position of state (ii) depends on shell interaction, and can be at any point along the post-snapping curve in Figure 3A, even at sites approaching state (iii). If snapping brings state (ii) to coincide with state (iii) (red point), then the volume change and the stored energy of the spherical cap reach the maximum values, $\Delta V_{\text{upper}}^*$ and $\Delta U_{1(\text{upper})}^*$ (Figure 3A), which are the upper bounds illustrated in Figure 3A respectively in the lower part and in cyan. At this state, the energy released by the bi-shell valve, $\Delta U_{\text{upper}}^* = p_i \Delta V_{\text{upper}}^* - \Delta U_{1(\text{upper})}^*$, also reaches the upper bound, (see the Supporting Information for details). $\Delta V_{\text{upper}}^*$ and $\Delta U_{\text{upper}}^*$ describe an ideal scenario for bi-shell valve where the pressure of the imperfect shell is insensitive to snapping, i.e., no pressure

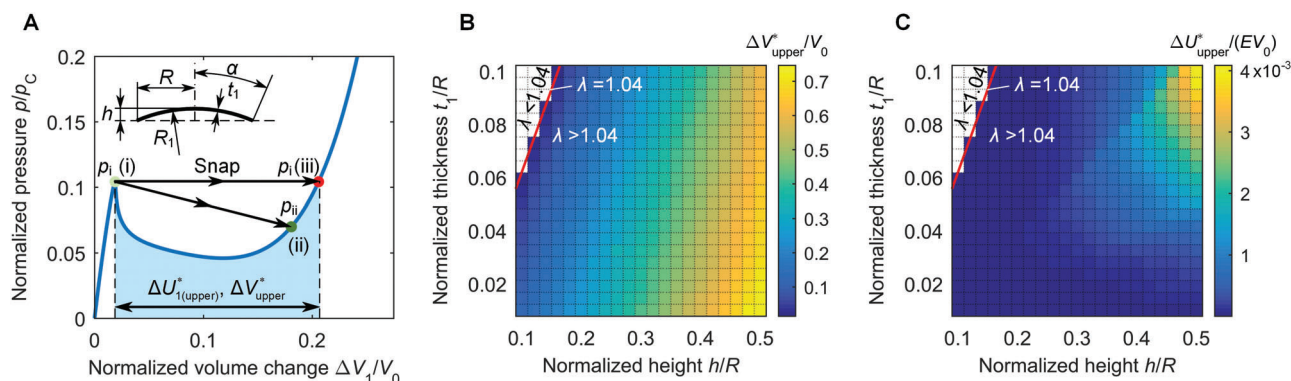


Figure 3. Upper bounds of performance for perfect shell limiting our bi-shell valve output. A) Representative pressure-volume curve of a perfect spherical shell. B) Upper bound of volume change, $\Delta V_{upper}^*/V_0$, plotted as a function of the normalized thickness t_1/R and normalized height h/R . C) Upper bound of released energy of the bi-shell valve, $\Delta U_{upper}^*/(EV_0)$, plotted as a function of t_1/R and h/R . $\lambda = (12(1 - \nu^2))^{1/4}(R_1/t_1)^{1/2}\alpha$ with ν the Poisson's ratio. Normalization factors of the volume change and released energy are V_0 , the volume of a hemisphere with radius R , and, Young's modulus E .

drop is developed during snapping and no change in pressure takes place (see the Supporting Information for details). In the following, we show that the upper bounds obtained for the perfect spherical cap can be used to characterize the output performance of our bi-shell valve as a function of the cap geometry.

To assess the snapping performance with respect to changes in shell geometry, we first define a widely used parameter of the perfect cap shape, which incorporates the dimensionless size and thickness of the spherical cap. This is $\lambda = (12(1 - \nu^2))^{1/4}(R_1/t_1)^{1/2}\alpha$,^[50,51] where R_1 is the radius of the spherical cap, t_1 is the thickness, α (Figure 3A) is the edge angle measured from the axis of symmetry, and ν the Poisson ratio. λ enables for the discrimination of areas of the design space, normalized thickness t_1/R versus normalized height h/R , with snap-through instability from those without. This is illustrated (Figure 3B,C) for both upper bounds of volume change and released energy. For $\lambda < 1.04$ (white area in the upper left corner), the spherical cap is thick and shallow, and no snap-through takes place; here there is only shell deflation with a smooth increase of pressure that cannot generate any rapid volume change. In contrast for $\lambda > 1.04$, the shell, thinner and deeper in geometry, undergoes snap-through for all combinations of t_1/R and h/R . As per the values of the upper bounds for volume change and released energy, the results in Figure 3B,C help to gain insights into the geometric parameters that govern the output performance of the bi-shell valve. From their contour plots, we observe that ΔV_{upper}^* increases monotonically with the normalized height h/R and its span is sizeable, from $\Delta V_{upper}^*/V_0 = 0$ to 0.75 (Figure 3B). The main implications is that a shell with higher h/R in its initial state, inherently encloses a larger inner volume, thus outlining a geometry capable of generating large change in volume upon snapping to the fully everted state. On the other hand, compared to h/R , the normalized thickness t_1/R exerts a minor influence on the volume change. As per the energy release, Figure 3C shows that ΔU_{upper}^* increases from $\Delta U_{upper}^*/(EV_0) = 0$ to 0.004 with both h/R and t_1/R . In comparison, shells with larger h/R can generate more ample change in volume during snapping, with a larger t_1/R providing a higher pressure. The maximum released energy $\Delta U_{upper}^*/(EV_0)$ is obtained at the upper right corner of Figure 3C, where both h/R

and t_1/R take their largest values, and both volume and pressure changes have large values.

The results in Figure 3B,C become useful for soft robotic applications. ΔV_{upper}^* and ΔU_{upper}^* set performance limits that apply to our bi-shell valve. h/R and t_1/R are the governing dimensionless parameters. Through the proper combination of their h/R and t_1/R , we can program the max volume change and released energy of the valve from the geometry of the cap only. For example, a sufficiently large h/R is needed to generate enough volume change and energy for soft actuators, whereas a small h/R can limit the upper bound of volume change ΔV_{upper}^* and released energy ΔU_{upper}^* to within a safety threshold, e.g., to prevent accident in human-robot interaction.^[52] On the other hand, the normalized thickness t_1/R has low to mild influence on the volume change ΔV_{upper}^* , but strong on the upper bound of the released energy ΔU_{upper}^* .

2.5. Bi-Shell Valve Performance in Service: Attainable Values of Volume Change and Released Energy

While the cap snapping bounds the theoretical output of the bi-shell valve ΔV_{upper}^* and ΔU_{upper}^* (top sketch in Figure 4A), it is the interaction between the two shells that governs the values of volume change ΔV^* and energy ΔU^* that the bi-shell system can actually release during operation (low sketch in Figure 4A). Our goal here is to find this second set of metrics (ΔV^* and ΔU^*) defining our bi-shell valve performance. We do so by first prescribing the geometry of the spherical cap ($t_1/R = 0.05$, $h/R = 0.2$, and $R = 25\text{mm}$), and then systematically exploring the design space of the imperfect shell. This step entails finding the range of ΔV^* and ΔU^* that can be obtained by varying the normalized thickness, t_2/R , within a representative span (0.02–0.1), and the meridional angles of the upper and lower boundaries, θ_U and θ_L , from 20° to 85°, a demonstrative range that we select here for these angles.

Figure 4B shows the attainable volume change $\Delta V^*/\Delta V_{upper}^*$ (blue plot) and released energy $\Delta U^*/\Delta U_{upper}^*$ (orange plot) as a function of t_2/R , the normalized thickness of the imperfect shell,

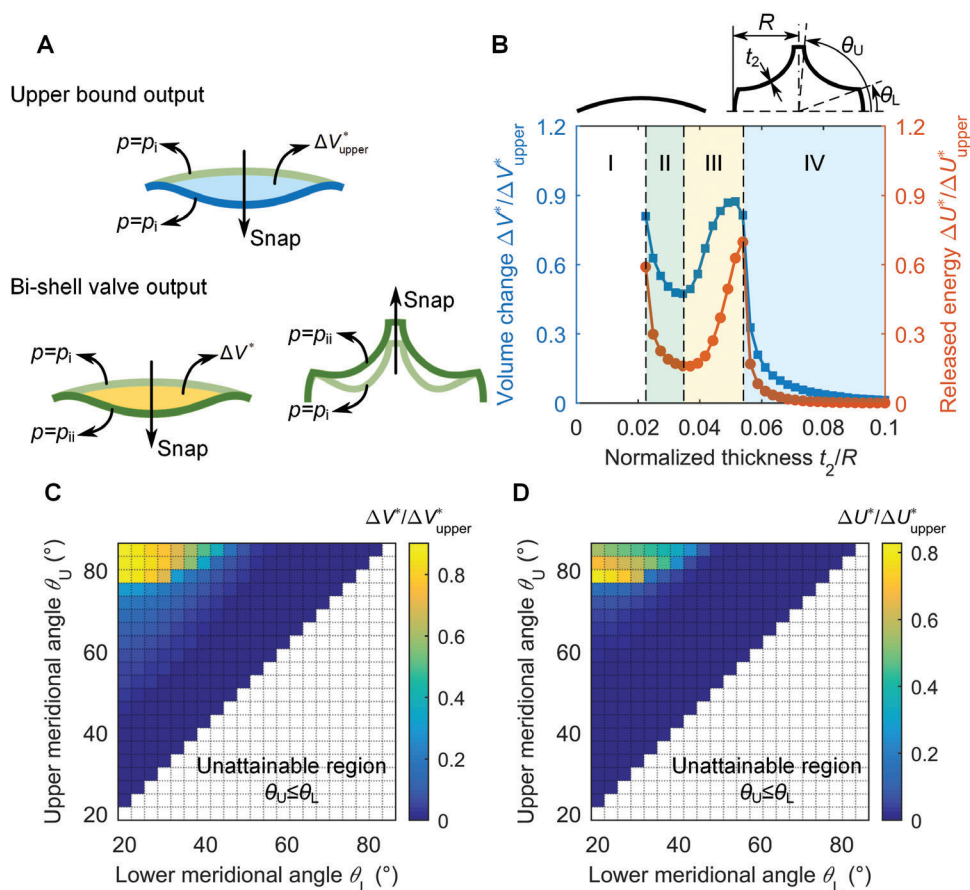


Figure 4. Bi-shell valve output. A) Upper bound output at $p = p_i$ and bi-shell valve output at $p = p_{ii}$. B) Performance output of bi-shell valve as a function of the normalized thickness t_2/R of the imperfect shell for given geometry of the spherical cap. C) Volume change, $\Delta V^*/\Delta V^*_{upper}$, as a function of the meridional angles defining the upper and lower boundary of imperfection, θ_U and θ_L . D) Released energy, $\Delta U^*/\Delta U^*_{upper}$, as a function of the meridional angles defining the upper and lower boundary of imperfection, θ_U and θ_L . Normalization factors of the volume change and released energy are the upper bounds ΔV^*_{upper} and ΔU^*_{upper} . The unattainable region in white corresponds to cases where θ_U is below or equal to θ_L .

for given meridional angles ($\theta_U = 85^\circ$ and $\theta_L = 20^\circ$). Here we can identify four regimes, each yielding a distinct performance of the bi-shell valve (see the Supporting Information S5 for the analysis of the buckling modes). For $t_2/R \leq 0.02$ (regime I), no snapping occurs because the imperfect shell is much more compliant than the spherical cap and collapse brings it to full eversion before the pressure is able to reach the snapping pressure of the spherical cap. For $0.02 < t_2/R < 0.035$ (regime II), the volume change ΔV^* decreases with t_2/R from 81% to 47% of the upper bound ΔV^*_{upper} , and the released energy ΔU drops from 59% to 16% of the upper bound ΔU^*_{upper} . Within this range, the minimum values of ΔV and ΔU are low compared to the upper bounds generated by the spherical cap; this implies that the imperfect shell can only trigger a small portion of ΔV^*_{upper} and ΔU^*_{upper} . On the other hand, in regime III ($0.035 < t_2/R < 0.055$), both the volume change and released energy of the bi-shell valve increase rapidly with t_2/R . The volume change ranges from $\Delta V^*/\Delta V^*_{upper} = 0.49$ to 0.87 and the released energy ($\Delta U^*/\Delta U^*_{upper}$) spans the range 0.16–0.70. A further increase in t_2/R (regime IV) leads to an abrupt drop in both volume change and released energy, followed by a plateau that

gradually approaches the value of zero. For these shells, snapping offers very modest volume change and released energy.

If the meridional angles, θ_U and θ_L , are both considered as design parameters, then a larger design space emerges for both $\Delta V^*/\Delta V^*_{upper}$ and $\Delta U^*/\Delta U^*_{upper}$. This is shown respectively in Figure 4C,D. Here the normalized thickness is prescribed to the value $t_2/R = 0.05$ to ensure that $\Delta V^*/\Delta V^*_{upper}$ and $\Delta U^*/\Delta U^*_{upper}$ can take the largest output depicted in Figure 4B. In terms of volume change $\Delta V^*/\Delta V^*_{upper}$, the yellow upper left corner in Figure 4C indicates large values, whereas the other regions in blue show a modest volume change $\Delta V^*/\Delta V^*_{upper}$ almost close to zero. For $\theta_L \leq 33^\circ$, we find that the volume change $\Delta V^*/\Delta V^*_{upper}$ first increases slowly with the upper meridional angle θ_U until an abrupt increase from $\Delta V^*/\Delta V^*_{upper} = 0.3$ to 0.9 appears at $\theta_U = 78.5^\circ$. With further increase in θ_U , the volume change $\Delta V^*/\Delta V^*_{upper}$ stays almost constant for the plotted range $\theta_U \leq 85^\circ$. As per the released energy, Figure 4D shows a contour plot similar to that of the volume change (Figure 4C). For $\theta_L \leq 33^\circ$, an abrupt increase of released energy from $\Delta U^*/\Delta U^*_{upper} = 0.15$ to 0.83, the maximum, appears at $\theta_U = 78.5^\circ$. A further increase in θ_U ,

however, yields reduced values of the released energy, as opposed to $\Delta V^*/\Delta V_{\text{upper}}^*$ which remains almost constant for $\theta_U \geq 78.5^\circ$. As with Figure 4B, the maximum values of the volume change ΔV^* and released energy ΔU^* in Figure 4C,D can only be attained in a narrow design space (yellow) of the imperfect shell. This zone is key to maximize the valve output, i.e., to release a large amount of energy. Its extent is governed by the interaction between the spherical cap and the imperfect shell. In particular, this yellow zone describes bi-shell valves in which the plateau pressure of the imperfect shell is located between the pre and post-snapping pressure p_i and p_{ii} of the spherical cap (see the Supporting Information for further details).

In summary, the upper bounds ($\Delta V_{\text{upper}}^*$ and $\Delta U_{\text{upper}}^*$) in Figure 3 and the valve outputs (ΔV^* and ΔU^*) in Figure 4 provide guidelines of practical use for the design of our bi-shell valve. First, the upper bounds in Figure 3 can guide the selection of the spherical cap that has the potential to generate a proper valve output. Second, for a given spherical cap, Figure 4 (along with Figure S13, Supporting Information) summarizes the range of valve output that can be tuned with the geometry of the imperfect shell as well as identifies distinct regimes of buckling modes. In this case, despite the size of the design space, only a small window is available for the imperfect shell (yellow area in the upper left corner of Figure 4C,D) to generate a valve output that is close to the upper bound. The insights here gained point out that $\theta_U = 85.9^\circ$ and $\theta_L = 20^\circ$ are among the best geometric parameters of the imperfect shell that can elicit the large volume change that we observe in our experiments (Figure 2 and Movie S1, Supporting Information). While the results in Figure 4 mapping the geometric role of the imperfect shell are for a specific geometry of the spherical cap, our analysis can be straightforwardly applied to spherical caps with other geometries; this merely requires updating the spherical cap geometry and replot the bi-shell valve performance of Figure 4.

2.6. Application of the Bi-Shell Valve

We now capitalize on the performance assessment and physical insights gained so far to demonstrate the capacity of our bi-valve to leverage shell snapping interaction for rapid actuation of fluidic soft actuators. As illustrative application, we employ a soft pneumatic striker that we actuate through our bi-shell valve. The goal is to make the striker suddenly move in response to the concerted snapping of the valve shells, deflated merely with slow volume input, propelling a table tennis ball along a guided track.

Figure 5A illustrates the schematic of our "soft punch" system. It consists of an airbag that contracts upon deflation and a paper stick that is driven by the airbag to hit and drive the table tennis ball along a slotted rail. Below the airbag, a pivot is fixed to the slotted rail at its midpoint, around which the paper stick can swing freely through the air. The system works as follows. First, the bi-shell valve is deflated to a state near to its pre-snapping state; during this process, the elastic strain energy is stored in the shells interacting through their input chamber. Second, the airbag is connected to the output chamber. Third, further deflation is applied at a low flow rate; this enables the pressure in the input chamber underneath the shells to reach the buckling load of the spherical cap. At this stage, the spherical

cap snaps downward and swiftly engages its imperfect counterpart to snap upward. Shell cooperation is now capitalized. The elastic energy and volume change hoarded in the imperfect shell before snapping is now released to propel fast deflation of the spherical cap. Since the output chamber surrounding the spherical cap connects to the airbag, the accrued rapid volume change is dispensed to fast deflate the airbag (Figure 5B). Since the tubing connecting the valve and soft actuator is short, the flow resistance or backpressure of the tubing is negligible. As a result, the upper part of the stick retracts and swings backward around the pivot, whereas its lower portion knocks the ball forward, away from its initial position.

Figure 5C,D shows the physical realization of the schematics shown in Figure 5A,B. In Figure 5C, the airbag is connected through a tube to the output chamber of our bi-shell valve (Figure 5A), while a syringe inflates the airbag from its natural flat condition to its fully inflated state. Once full inflation is reached, the syringe ceases to provide any increase of air volume. Deflation of the input chamber at the inlet is at a constant flow rate of 3 mL min^{-1} . After snapping, the airbag deflates almost instantly until air exhaustion, a condition where the air bag becomes fully rigid. The absence of air in the airbag impedes the spherical cap to reach full eversion, rather only a dimple forms on its top (Figure 5D). Despite full eversion is not being attained, the partial snapping enables the striker to hit the table tennis ball up to 3 cm from its initial position (Movie S2, Supporting Information). We emphasize that if the bi-shell valve cannot generate sufficient volume change to meet the requirements of a given soft robotic application, e.g., when the stiffness of the actuator influences the bi-shell valve output, then the valve design (see Figure S16 for design flow chart in the Supporting Information) can be readjusted through the metrics introduced in the maps of Figures 3 and 4. This shows a versatile design for our valve capable of matching the actuator performance, and reaching the target volume change regardless of the actuator performance.

Figure 5E shows the displacement and velocity imparted by the striker to the table tennis ball. Before actuation, the ball rests in its initial position with both displacement and velocity equal zero. This reflects the condition of the airbag being not deflated. Upon snapping, the ball quickly accelerates to reach a speed of 58 mm s^{-1} within 0.16 s. After actuation, the ball keeps moving on the rail until the speed gradually declines to zero, due to the combined effects of rail friction, rail unevenness and air drag.

To further prove that the fast movement of the striker is enabled by our bi-shell valve, we perform two additional tests that compare the striker actuation in two scenarios (Figure 6): one with the bi-shell valve and the other without the valve. In this set of tests, we focus on the response of the striker only, and hence we remove the table tennis ball and the rail. For the first test (Figure 6A–D), we connect the striker to the bi-shell valve and slowly deflate the valve at a constant flow rate of 3 mL min^{-1} . The airbag quickly deflates within 0.16 s upon snapping (Movie S3, Supporting Information), a result in agreement with the time required by the table tennis ball to accelerate. For the second test (Figure 6E–H), we remove the bi-shell valve and directly deflate the airbag at the identical flow rate (3 mL min^{-1}). What we observe here is that the airbag slowly shrinks to the fully deflated state over about 13 s (Movie S4, Supporting Information), i.e., roughly 80 times slower than the first scenario. The comparison of these test results

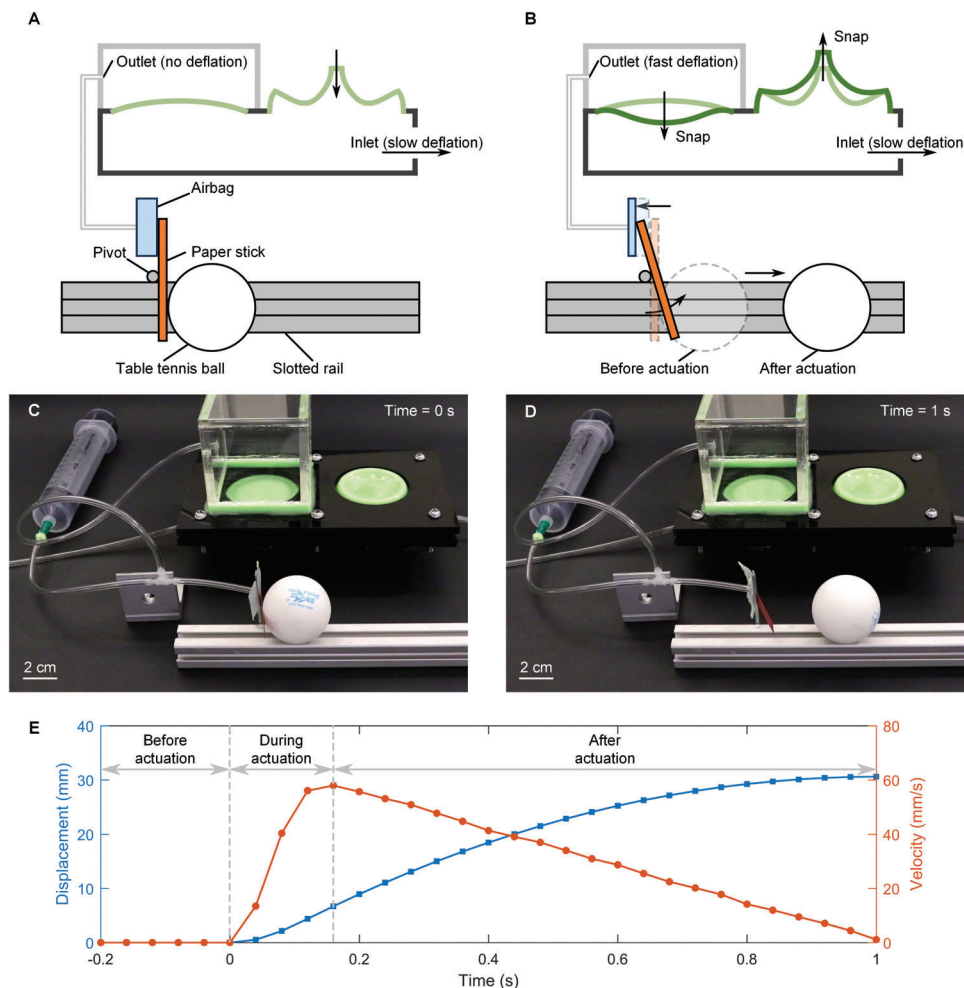


Figure 5. A striker rapidly actuated by bi-shell valve to propel motion of table tennis ball. A) The striker consists of an airbag and a paper stick. The airbag is connected to the bi-shell valve. The paper stick is constrained by a pivot fixed to the slotted rail to enable swinging around its midpoint. A table tennis ball placed on the slotted rail is in contact with the paper stick. B) Upon snapping of the bi-shell valve, the airbag rapidly deflates to swing the paper stick, which rotates anti-clockwise to hit the ball along the rail. C, D) Photographs prior and post the striker hit (Movie S2, Supporting Information). A syringe is used to inflate the airbag from its natural flat condition to its fully inflated state; it ceases to provide any increase of air volume once full inflation is reached. E) Displacement and velocity of the table tennis ball as a function of time. Time = 0 s is the instant when the striker is actuated by the bi-shell valve.

attests that our bi-shell valve is responsible for the fast movement of the striker. In summary, the experiments above demonstrate that our bi-shell valve can achieve fast actuation through a slow volume input. While existing snapping valves^[22,29,43–45] can provide binary control of a given flow, our concept leverages shell cooperation and snapping interaction to quickly impart a fast volume change that can be used for actuation.

2.7. Discussion

Widely used methods currently available for rapid actuation mainly resort to pressure-controlled strategies that require a bulky system of pressure supply, sensors, hard valves, and control algorithms.^[4,15] Other methods to achieve rapid actuation either employ explosive chemical reaction^[39–42] or exploit a structural

instability embedded within the actuator, which would require the integration of snapping spherical caps^[31] or balloons^[32,36,37] into the architecture of the actuator. In contrast, our bi-shell valve does not rely on the fast volume input from pressure control or any modifications to the actuator design. It can be easily implemented with a simple volume input dispensed through a syringe and connected to an existing actuator. We note that the pressure output is governed by the constituent shells. In this work, the snapping pressure of the bi-shell valve is in the range 405–549 Pa (Figure S6, Supporting Information). Yet, the snapping pressure can be increased by stiffening the shells. On this front, two strategies can be followed. One is to thicken the shell and scale up the snapping pressure to a value as large as 10 kPa, as demonstrated in the literature.^[29] Another way is to choose a material with Young's modulus higher than that of our prototype valve (see the Supporting Information for details). Both methods can

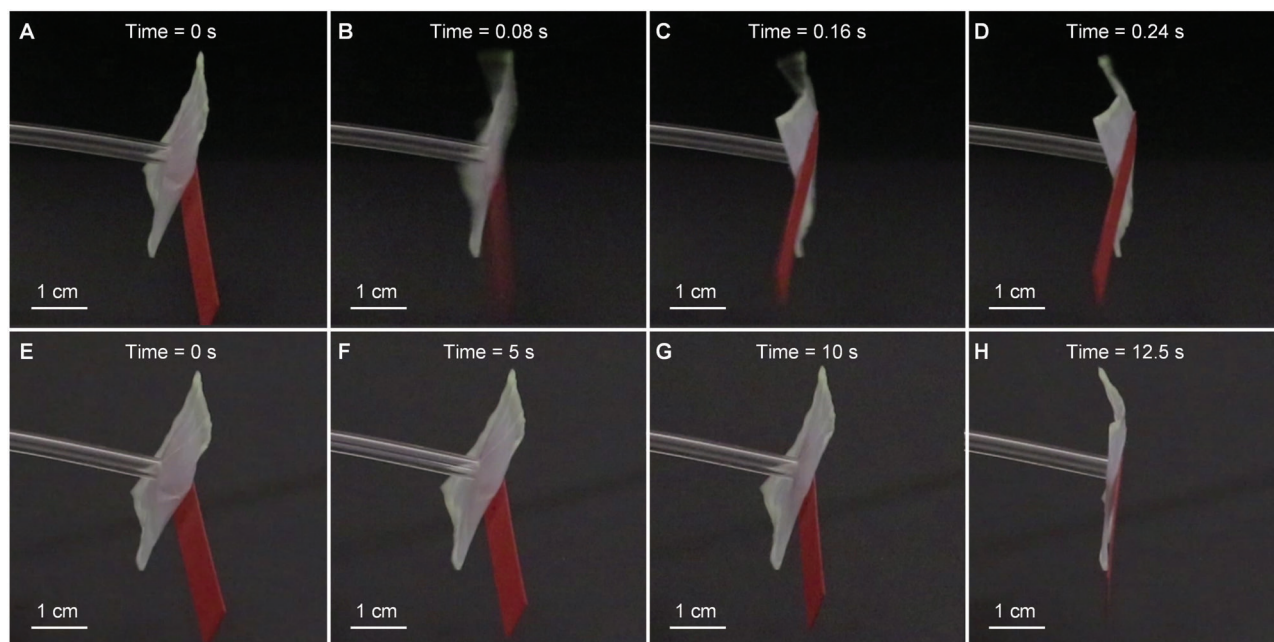


Figure 6. A–D) Fast actuation of the striker enabled by the bi-shell valve. The striker can reach full deflation in 0.16 s and reach a state with no intrinsic vibration at 0.24 s. E–H) Slow actuation of the striker due to the absence of the bi-shell valve. More than 10 s are required for actuation. For both tests, the actuation time is counted from the 0 s instant.

be used either individually or in combination to further amplify the pressure output and meet the design requirements imposed by the application.

In addition, our valve performance could not be achieved by employing one single shell, as in existing valve designs delivering mainly fluid control function.^[22,29,43–45] The reason is that the flow rate difference between the valve input and the valve output is enabled by the volume rapidly transferred between the constituent shells during snapping. This allows to convert the low flow rate at the inlet to a fast flow rate at the outlet. If only one shell were used, either the spherical cap or the imperfect shell, no fast actuation would be attainable because there would be no means in place for flow-rate conversion, i.e., no fast transfer of air volume can be accomplished. Another advantage is the self-adaptivity of its volume output to that of the actuator. Our experiments have shown that the valve can be autonomously adjusted to yield a volume output that is compatible with the volume of the actuator at the outlet, hence preventing the actuator from any possible damage caused by excessive deflation. Furthermore, the hyperelastic constitutive law of the shell base-material guarantees reversible and repetitive snapping imposed by a cyclic loop of deflation and inflation (Movie S5, Supporting Information), which is common for soft robots and actuators.^[29,31] In our demonstration, the choice to show the bi-shell valve on a system containing rigid components is only for the convenience to observe the snapping event and the interaction of the constituent shells. To integrate our valve within a soft robot, the output chamber can be merged with the interior of the soft actuator, while the whole system of the bi-shell valve and the soft actuator can be controlled from the input chamber. A possible layout of the valve-actuator integration is given in Figure S19 (Supporting Information). Both the rigid input and output

chambers can be replaced with thick soft walls by molding.^[29] The integration would only require the merging of both molds, that of the bi-shell valve and that of the soft actuator.

While our current concept is devised mainly to attain rapid deflation, the potential to embed more functions is at hand. For example, the bi-shell valve can be designed as a fuse of volume change by placing the output chamber above the imperfect shell, rather than on the spherical cap (Figure S17, Supporting Information). In this case, the volume output will initially increase with the volume input until a threshold is reached; at this stage the imperfect shell inflates with the snapping of the valve. Another example is the potential to swap deflation (negative pressure) with inflation (positive pressure). Several pneumatic robots are actuated by inflation rather than deflation. By flipping the imperfect shell and the spherical cap upside down (Figure S17, Supporting Information), our bi-shell valve can be reset to operate under inflation. Compared to existing valves^[43,45,53] that are capable of continuous operation, the bi-shell valve and the variational designs for inflation here presented can provide an impulse output with finite volume (Figure 4C). At the design stage, it is necessary to ensure that such an impulse can provide the volume change that is sufficient to fast actuate the soft actuator. Moreover, while the bi-shell valve presented here provides a simple task for fast actuation, more complex logic functions could be achieved by integrating the valve into the fluidic system of circuits of a soft robot.^[22,23,29,44]

3. Conclusion

To achieve rapid actuation of soft pneumatic actuators, we have introduced a soft bi-shell valve that can convert a slow volume input into a fast output. The underpinning principle is the

Received: February 2, 2021

Revised: March 25, 2021

Published online:

interaction during snap-through of its elastic soft constituents: an imperfect shell and a spherical cap. Upon deflation, the former first stores sizeable values of volume change and elastic energy, which are then suddenly released upon snapping of the latter. Its rapid volume output can be used to deliver fast actuation. Upper bounds and performance metrics have been presented to design the bi-shell valve for target requirements of soft robotic applications. The spherical cap determines the snapping pressure and the upper bounds of volume change and released energy, while the imperfect shell interacts with the cap to yield an attainable valve output. Tuning defect geometry and shell shape enables to passively code the snapping event, calibrate volume and energy output and maximize the valve performance. Through the demonstration of the striker, we have shown that the bi-shell valve can accelerate the motion of soft actuators under volume control, thus avoiding the need for fast volume input provided by pressure control nor additional modifications to the body of the actuator that use chemical explosion or elastic instability. In conclusion, the bi-shell valve concept introduced in this work along with its variational designs are poised to offer new routes to provide actuation of soft pneumatic actuators.

4. Experimental Section

Methods: Section S1 in the Supporting Information details the fabrication methods, while the experimental characterization of the bi-shell valve and the elastic shells are described in Section S2 in the Supporting Information. The effect of air compressibility is discussed in Section S3 (Supporting Information). Section S4 (Supporting Information) reports the numeric analysis. Sections S5 to S7 (Supporting Information) discuss the buckling modes of the imperfect shell, the interaction between the spherical cap and the imperfect shell, and the upper bounds of valve output. The flowchart detailing the valve design as well as design variations of the bi-shell concept are presented in Sections S8 and S9 (Supporting Information). The effects of material property are studied in Section S10 (Supporting Information). Section S11 (Supporting Information) presents a possible layout for the integration of the bi-shell valve into a soft robot or actuators, and Section S12 (Supporting Information) discusses the scenario of a similar valve with only one shell.

Supporting Information

Supporting Information is available from the Wiley Online Library or from the author.

Acknowledgements

This work was supported by the Natural Sciences and Engineering Research Council of Canada, Grant # 208241.

Conflict of Interest

The authors declare no conflict of interest.

Data Availability Statement

Data available on request from the authors.

Keywords

actuation methods, elastic instabilities, fast actuation, snap-through buckling, soft pneumatic actuators, soft robots, soft valves

- [1] D. Rus, M. T. Tolley, *Nature* **2015**, 521, 467.
- [2] G. M. Whitesides, *Angew. Chem., Int. Ed.* **2018**, 57, 4258.
- [3] J. H. Pikul, S. Li, H. Bai, R. T. Hanlon, I. Cohen, R. F. Shepherd, *Science* **2017**, 358, 210.
- [4] E. Siéfert, E. Reyssat, J. Bico, B. Roman, *Nat. Mater.* **2019**, 18, 24.
- [5] E. W. Hawkes, L. H. Blumenschein, J. D. Greer, A. M. Okamura, *Sci. Rob.* **2017**, 2, eaaz3028.
- [6] N. S. Usevitch, Z. M. Hammond, M. Schwager, A. M. Okamura, E. W. Hawkes, S. Follmer, *Sci. Rob.* **2020**, 5, eaaz0492.
- [7] H. Li, J. Yao, C. Liu, P. Zhou, Y. Xu, Y. Zhao, *Soft Rob.* **2020**, 7, 491.
- [8] Y. Tang, Y. Chi, J. Sun, T.-H. Huang, O. H. Maghsoudi, A. Spence, J. Zhao, H. Su, J. Yin, *Sci. Adv.* **2020**, 6, eaaz6912.
- [9] Y. Tang, J. Yin, *Adv. Mater. Technol.* **2018**, 3, 1800069.
- [10] L. Qin, X. Liang, H. Huang, C. K. Chui, R. C.-H. Yeow, J. Zhu, *Soft Rob.* **2019**, 6, 455.
- [11] A. Seibel, L. Schiller, *Robot. Biomimetics* **2018**, 5, 5.
- [12] Y. Tang, Q. Zhang, G. Lin, J. Yin, *Soft Rob.* **2018**, 5, 592.
- [13] M. S. Verma, A. Ainla, D. Yang, D. Harburg, G. M. Whitesides, *Soft Rob.* **2017**, 5, 133.
- [14] J. Shintake, V. Cacucciolo, D. Floreano, H. Shea, *Adv. Mater.* **2018**, 30, 1707035.
- [15] Z. Xie, A. G. Domel, N. An, C. Green, Z. Gong, T. Wang, E. M. Knubben, J. C. Weaver, K. Bertoldi, L. Wen, *Soft Rob.* **2019**, 7, 639.
- [16] A. Ainla, M. S. Verma, D. Yang, G. M. Whitesides, *Soft Rob.* **2017**, 4, 297.
- [17] P. Polygerinos, K. C. Galloway, E. Savage, M. Herman, K. O. Donnell, C. J. Walsh, in *IEEE Int. Conf. on Robotics and Automation (ICRA)*, IEEE, Piscataway, NJ **2015**.
- [18] J. Fang, J. Yuan, M. Wang, L. Xiao, J. Yang, Z. Lin, P. Xu, L. Hou, *Soft Rob.* **2020**, 7, 95.
- [19] C. Paul, *Rob. Auton. Syst.* **2006**, 54, 619.
- [20] H. Hauser, A. J. Ijspeert, R. M. Fuchsli, R. Pfeifer, W. Maass, *Biol. Cybern.* **2011**, 105, 355.
- [21] P. Polygerinos, N. Correll, S. A. Morin, B. Mosadegh, C. D. Onal, K. Petersen, M. Cianchetti, M. T. Tolley, R. F. Shepherd, *Adv. Eng. Mater.* **2017**, 19, 1700016.
- [22] D. J. Preston, P. Rothemund, H. J. Jiang, M. P. Nemitz, J. Rawson, Z. Suo, G. M. Whitesides, *Proc. Natl. Acad. Sci. USA* **2019**, 116, 7750.
- [23] M. Wehner, R. L. Truby, D. J. Fitzgerald, B. Mosadegh, G. M. Whitesides, J. A. Lewis, R. J. Wood, *Nature* **2016**, 536, 451.
- [24] T. Ranzani, S. Russo, N. W. Bartlett, M. Wehner, R. J. Wood, *Adv. Mater.* **2018**, 30, 1802739.
- [25] D. Yang, M. S. Verma, J.-H. So, B. Mosadegh, C. Keplinger, B. Lee, F. Khashai, E. Lossner, Z. Suo, G. M. Whitesides, *Adv. Mater. Technol.* **2016**, 1, 1600055.
- [26] B. Mosadegh, P. Polygerinos, C. Keplinger, S. Wennstedt, R. F. Shepherd, U. Gupta, J. Shim, K. Bertoldi, C. J. Walsh, G. M. Whitesides, *Adv. Funct. Mater.* **2014**, 24, 2163.
- [27] S. Russo, T. Ranzani, C. J. Walsh, R. J. Wood, *Adv. Mater. Technol.* **2017**, 2, 1700135.
- [28] Y.-F. Zhang, C. J.-X. Ng, Z. Chen, W. Zhang, S. Panjwani, K. Kowsari, H. Y. Yang, Q. Ge, *Adv. Mater. Technol.* **2019**, 4, 1900427.
- [29] P. Rothemund, A. Ainla, L. Belding, D. J. Preston, S. Kurihara, Z. Suo, G. M. Whitesides, *Sci. Rob.* **2018**, 3, eaar7986.
- [30] E. Ben-Haim, L. Salem, Y. Or, A. D. Gat, *Soft Rob.* **2019**, 7, 259.
- [31] B. Gorissen, D. Melancon, N. Vasios, M. Torbati, K. Bertoldi, *Sci. Rob.* **2020**, 5, eabb1967.

- [32] J. T. B. Overvelde, T. Kloek, J. J. A. D'haen, K. Bertoldi, *Proc. Natl. Acad. Sci. USA* **2015**, *112*, 10863.
- [33] E. Milana, B. Gorissen, M. D. Volder, D. Reynaerts, in *IEEE Int. Conf. on Soft Robotics (RoboSoft)*, IEEE, Piscataway, NJ **2018**.
- [34] C. Keplinger, T. Li, R. Baumgartner, Z. Suo, S. Bauer, *Soft Matter* **2012**, *8*, 285.
- [35] T. Li, C. Keplinger, R. Baumgartner, S. Bauer, W. Yang, Z. Suo, *J. Mech. Phys. Solids* **2013**, *61*, 611.
- [36] L. Hines, K. Petersen, M. Sitti, *Adv. Mater.* **2016**, *28*, 3690.
- [37] R. Baumgartner, A. Kogler, J. M. Stadlbauer, C. C. Foo, R. Kaltseis, M. Baumgartner, G. Mao, C. Keplinger, S. J. A. Koh, N. Arnold, Z. Suo, M. Kaltenbrunner, S. Bauer, *Adv. Sci.* **2020**, *7*, 1903391.
- [38] M. Garrad, G. Soter, A. T. Conn, H. Hauser, J. Rossiter, in *2nd IEEE Int. Conf. on Soft Robotics (RoboSoft)*, IEEE, Piscataway, NJ **2019**.
- [39] R. F. Shepherd, A. A. Stokes, J. Freake, J. Barber, P. W. Snyder, A. D. Mazzeo, L. Cademartiri, S. A. Morin, G. M. Whitesides, *Angew. Chem., Int. Ed.* **2013**, *52*, 2892.
- [40] M. T. Tolley, R. F. Shepherd, M. Karpelson, N. W. Bartlett, K. C. Galloway, M. Wehner, R. Nunes, G. M. Whitesides, R. J. Wood, in *IEEE/RSJ Int. Conf. Intell. Robot. Syst.*, IEEE, Piscataway, NJ **2014**.
- [41] M. Loepfe, C. M. Schumacher, U. B. Lustenberger, W. J. Stark, *Soft Rob.* **2015**, *2*, 33.
- [42] N. W. Bartlett, M. T. Tolley, J. T. B. Overvelde, J. C. Weaver, B. Mosadegh, K. Bertoldi, G. M. Whitesides, R. J. Wood, *Science* **2015**, *349*, 161.
- [43] M. Gomez, D. E. Moulton, D. Vella, *Phys. Rev. Lett.* **2017**, *119*, 144502.
- [44] D. J. Preston, H. J. Jiang, V. Sanchez, P. Rothmund, J. Rawson, M. P. Nemitz, W.-K. Lee, Z. Suo, C. J. Walsh, G. M. Whitesides, *Sci. Rob.* **2019**, *4*, eaaw5496.
- [45] K. Luo, P. Rothmund, G. M. Whitesides, Z. Suo, *J. Mech. Phys. Solids* **2019**, *131*, 230.
- [46] J. W. Hutchinson, *Proc. R. Soc. London, Ser. A* **2016**, *472*, 20160577.
- [47] C. Qiao, L. Liu, D. Pasini, *J. Mech. Phys. Solids* **2020**, *141*, 103959.
- [48] W. Dreyer, I. Müller, P. Strehlow, *Q. J. Mech. Appl. Math.* **1982**, *35*, 419.
- [49] I. Müller, P. Strehlow, *Rubber and Rubber Balloons: Paradigms of Thermodynamics*, Springer, New York **2004**.
- [50] J. Paulose, D. R. Nelson, *Soft Matter* **2013**, *9*, 8227.
- [51] H. N. R. Wagner, C. Hühne, S. Niemann, *Int. J. Mech. Sci.* **2018**, *141*, 58.
- [52] S. Haddadin, A. Albu-Schäffer, G. Hirzinger, *Int. J. Rob. Res.* **2009**, *28*, 1507.
- [53] M. A. Unger, H.-P. Chou, T. Thorsen, A. Scherer, S. R. Quake, *Science* **2000**, *288*, 113.



Supporting Information

for *Adv. Sci.*, DOI: 10.1002/adv.202100445

Bi-shell valve for fast actuation of soft pneumatic actuators via shell snapping interaction

*Chuan Qiao, Lu Liu, Damiano Pasini**

Supporting Information

Bi-shell valve for fast actuation of soft pneumatic actuators via shell snapping interaction

*Chuan Qiao, Lu Liu, Damiano Pasini**

S1. Fabrication

S1.1. Fabrication of the input chamber

Figure S1 illustrates the manufacturing process for the input chamber encompassing six layers laser cut (CM1290 laser cutter, SignCut Inc., Canada) from a 6-mm-thick acrylic plate (McMaster-Carr, USA). The first layer at the bottom is fully solid with geometry parallel to the external profile of the two shells. From the second to the fifth layer the acrylic plates consists of a 15.5-mm-wide ring with an external profile identical to the first layer, forming the wall of the input chamber. Moreover, the third and fourth layers have an opening at both ends along their long axis, a feature that allows connection to the PVC plastic tubing for volume input and pressure sensor. The sixth layer at the top covers the input chamber enclosed by the first five layers, with two large circular holes that connect the imperfect shell and the spherical cap. In addition, six smaller holes on the top layer are used to fasten the input chamber with other parts of the bi-shell valve. Adhaero SuperGlue (Dollarama, Canada) is used to join all pieces of the input chamber assembly, and silicone rubber Elite double 32 (Zhermack, Italy) is applied to seal off its internal walls.

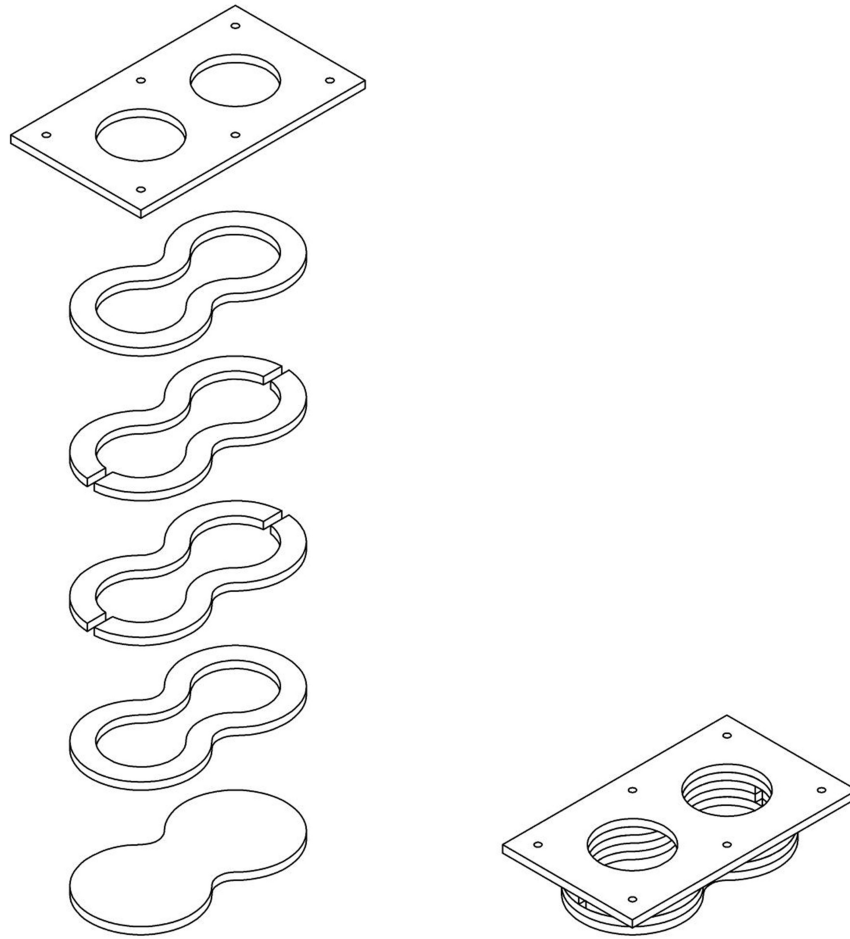


Figure S1. Assembly of the input chamber

S1.2. Fabrication of the output chamber

Figure S2 shows the output chamber consisting of five laser cut acrylic plates, which forms an open cubic cell that can capture the rapid volume change of the spherical cap. Again Adhaero SuperGlue (Dollarama, Canada) is applied to join the fives plates and Adhaero epoxy (Dollarama, Canada) is used to seal them. The small hole on the left-hand side of the cell provides the outlet of the output chamber, which in turn is connected through tubing to the soft actuator.

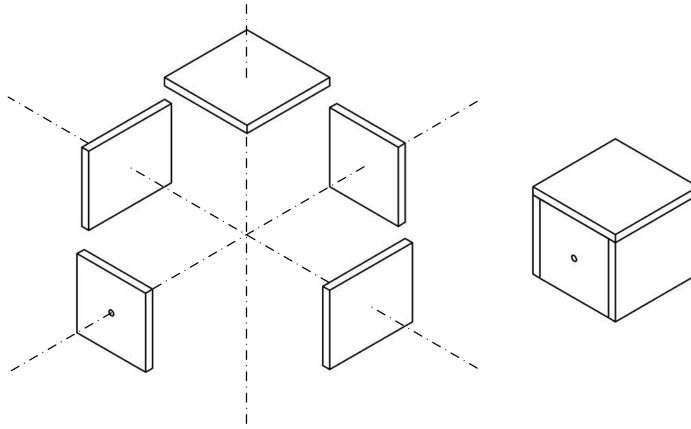


Figure S2. Assembly of the output chamber

S1.3. Fabrication of the elastic shells

Shell fabrication for both the imperfect shell and the spherical cap follows a procedure previously used.^[1, 2] Elite Double 32 (Zhermack, Italy) is casted on the surface of 3D-printed molds (Figure S3). For each shell, we fabricated a 1 mm-thick mold with Onyx filament using fused deposition modeling (FDM). The surface of the molds has geometry identical to that of the as-designed elastic shells ($R = 25 \text{ mm}$, $h/R = 0.2$, $\theta_L = 20^\circ$, and $\theta_U = 85.9^\circ$), with a groove at the bottom to collect excessive deposition of liquid and form a thick band that provide a clamping action. To locally reduce excessive accumulation of Elite Double 32 liquid on the curved surface of the mold, we used a homemade spin coating unit to spin the mold at a speed of $\sim 240 \text{ rpm}$. More specifically, the shells were fabricated at room temperature by following these steps:

- a) Prepare the catalyst and base of Elite Double 32 with 1:1 volume fraction.
- b) Mix and manually stir the prepared catalyst and base for $\sim 1 \text{ min}$.
- c) Turn on the power of the spin coating unit.
- d) Slowly pour the mixed Elite Double 32 solution onto the mold.
- e) Spin $\sim 10 \text{ min}$ to remove excessive liquid on the mold.

- f) Turn off the power of the spin coating unit.
- g) Wait about 15 min to fully cure the Elite Double 32 solution.
- h) Systematically increase shell thickness by repeating the above steps a) to g) until the designed thickness is attained.
- i) Repeat steps a) and b) and fill the groove at the bottom of the mold with mixed Elite Double 32 solution.
- j) Wait ~25 min until the Elite Double 32 solution is fully stabilized.
- k) Peel off the elastic shell from the mold.

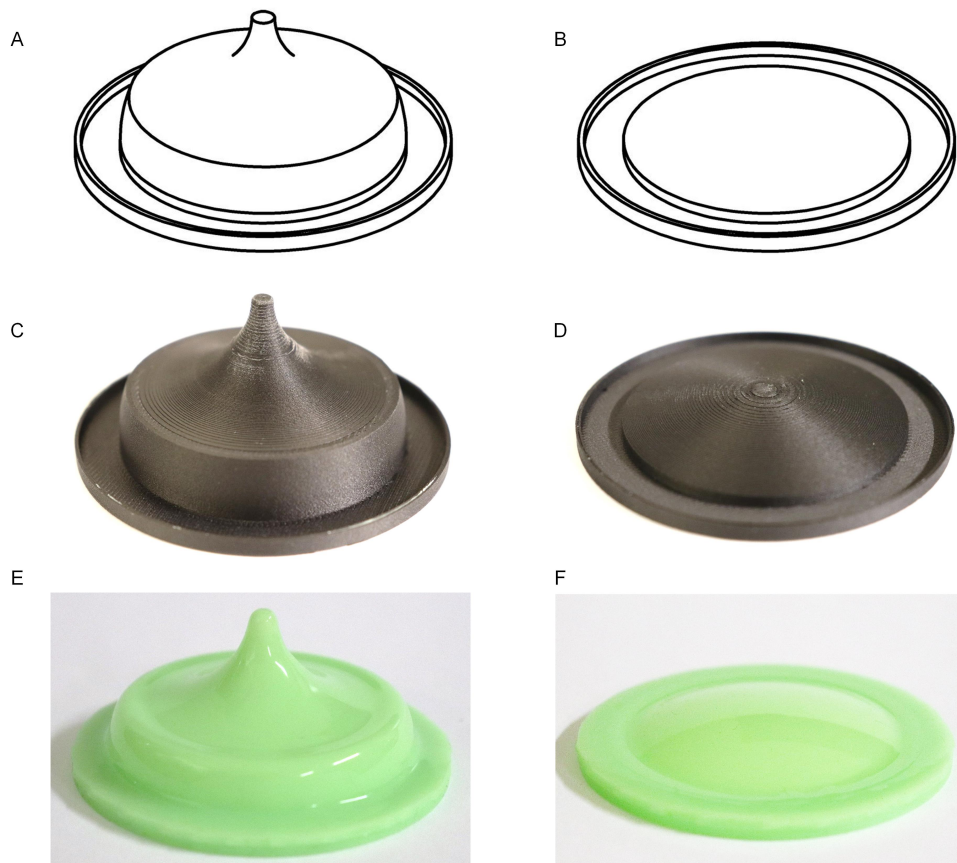


Figure S3. Mold for the imperfect shell and the spherical cap. (A) and (B): schematic of each respective mold. (C) and (D): 3D printed mold. (E) and (F): Fabricated shells.

S1.4. Assembly of the bi-shell valve

Figure S4 shows the components and assembly of our bi-shell valve system. The imperfect shell and the spherical cap are mounted on the input chamber, with their inner volume connected through the two large holes on the top surface of the input chamber. Any leakage that may exist between the elastic shells and the input chamber are sealed with Elite Double 32. Above the elastic shells is a fixture plate, which can be fastened to the input chamber with screws through six small holes along its edges. This fixture plate has two large circular holes that allow the elastic shells to freely deform without entering in contact with the fixture plate. Since the base of the spherical cap is thicker than that of the imperfect shell, the fixture plate can tightly clamp the base of the spherical cap on the input chamber to ensure airtight connection to the output chamber. The output chamber is mounted on the fixture plate with a square gasket made of Elite Double 32 that can tolerate the deformation of the fixture plate due to clamping. The leaks that may occur between the fixture plate and the output chamber are sealed with Elite Double 32 and Adhaero 5 minute epoxy (Dollarama, Canada).

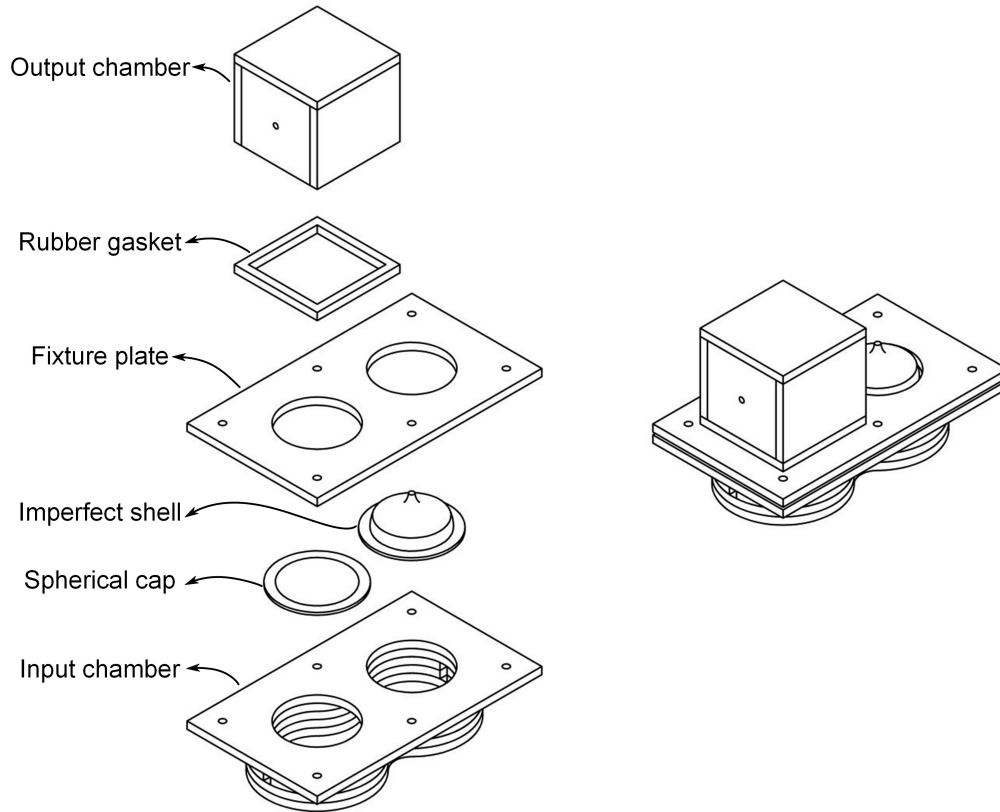


Figure S4. Components and assembly of the bi-shell valve system.

S1.5. Fabrication of the pneumatic striker

Our pneumatic striker consists of two main components: a miniature airbag to convert volume input into motion, and a paper stick to hit the table tennis ball. The airbag is cut from a 0.02-mm-thick compostable kitchen bag (no name, Loblaw's Inc, Canada) as a folded bi-layer film with an area of 28x28 mm. A segment of tubing is glued on the bottom surface of the cut film with Adhaero SuperGlue. A hole is then cut through the film to enable airflow between the airbag and the tubing. Finally, the airbag is sealed with Elite Double 32. The paper stick is cut from a 0.29-mm-thick paper and then glued on the top surface of the airbag with Elite Double 32. The length of the stick is 56 mm, and the width is 7 mm.

S2. Experimental characterization

S2.1. Characterization of a single shell

To characterize the pressure-volume response of a single shell, we assemble the experiment apparatus shown in Figure S5, which includes an acrylic fixture to hold the sample, a polypropylene syringe of 60 mL capacity to extract air from the sample, a Bose ElectroForce 3510 tester (Bose Corporation, Framingham, Massachusetts) to control the syringe, a pressure sensor (HSCDRRN002NDAA5, Honeywell, USA) that has a measurement range of ± 498 Pa and an accuracy of ± 2.5 Pa, and a microcontroller (Arduino UNO, Arduino, Italy).

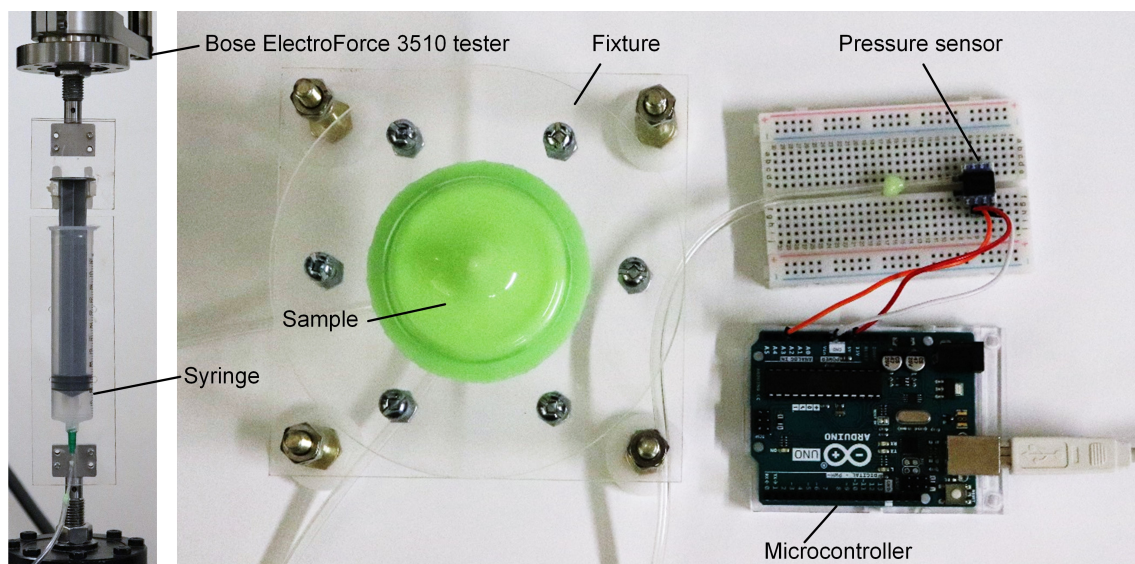


Figure S5. Experimental set-up for the characterization of a single shell.

The fixture consists of a top plate and a bottom plate. The top plate has a round geometry and is placed above the shell. There is a circular hole at the center, which not only allows the body of the shell to freely deform without entering in contact with the plate, but also clamps the base of the shell on the bottom plate. The bottom plate features a square geometry, and is connected to the syringe and the pressure sensor with a PVC plastic tubing. A 6-mm-thick ring gasket made of acrylic is glued at the center of the bottom plate, providing room for the spherical cap to fully deflate without getting into contact with the bottom plate. The top and

bottom plates can be tightly fastened with six equally spaced screws to prevent any air leakage.

In our test, the syringe is pulled by the Bose tester at a speed of 0.1 mm s^{-1} to generate a constant flow rate of 3 mL min^{-1} . The microcontroller is programmed to read the pressure measurement at a frequency of 20 Hz, which is then recorded as a function of time with a data acquisition software (PLX-DAQ, Parallax, USA). For both the spherical shell and the imperfect shell, three samples have been tested under identical conditions. The resulting curves (pressure-volume) along with the representative envelope of the experimental response of all tested samples are plotted in Figure 2E and 2F.

S2.2. Characterization of the bi-shell valve

Our experiment with the bi-shell valve is performed with the set-up described above for deflation and pressure measurement. The syringe and the pressure sensor are connected to the input chamber with the tubing at the bottom the valve. The flow rate of deflation is 3 mL min^{-1} , while the frequency of pressure measurement is 20 Hz. To assemble the bi-shell valve, we select one pair of spherical cap and imperfect shell from the pool of the single shell samples tested individually in the analyses of the previous sections. The result from the tests are shown in Figure S6. The results show that the snapping pressure of the valve can be programmed by the clamping condition of the spherical cap from 405 Pa when the spherical cap is not clamped (test 1), to 591 Pa when the spherical cap is tightly clamped (test 4). The increase in snapping pressure is caused by the initial deformation of the spherical cap due to clamping, a behaviour studied numerically in Supporting Information S4.1. The curve of test 2 corresponds to the results illustrated in Figure 2D with a snapping pressure identical to the test result of the individual spherical cap shown in Figure 2E. We assume that the initial deformation of the spherical cap in test 2 is identical to the initial deformation of the cap

when tested alone. The curve of test 3 corresponds to the bi-shell valve used in our demonstrative experiment, where the spherical cap buckles at 549 Pa. The higher snapping pressure of 591 Pa attained in test 4 is only used to show the role of a given clamping condition.

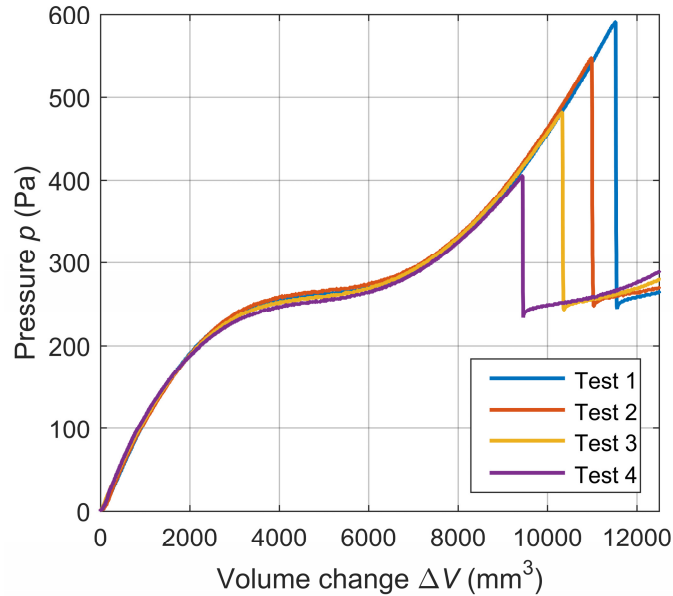


Figure S6. Pressure-volume response of the bi-shell valve. Pressure-volume response of the bi-shell valve. The spherical cap is not clamped in test 1 and tightly clamped in test 4, while tests 2 and 3 correspond to intermediate clamping conditions.

S3. Effect of air compressibility

Since air is a compressible fluid, here we study the influence of air compressibility. We assume that the air in the bi-shell-valve, the tubing, and the syringe follows the ideal gas law:

$$pV = nR_g T \quad (\text{S1})$$

where p is the pressure of the gas, V is the volume of the gas, n is the amount of substance of gas, R_g is the ideal gas constant, and T is the absolute temperature of the gas. In both the

initial state and loaded states. the gas in the pneumatic system (the bi-shell valve, syringe and connecting tubing) must satisfy

$$p_{sys0} V_{sys0} = nR_g T_{sys0} \quad (S2)$$

and

$$p_{sys1} V_{sys1} = nR_g T_{sys1} \quad (S3)$$

where the subscript stands for initial (0) and loaded states (1).

We assume the gas undergoes an isothermal process ($T_{sys0} = T_{sys1}$), which yields

$$p_{sys0} V_{sys0} = p_{sys1} V_{sys1} \quad (S4)$$

The volume change due to air compressibility can be expressed as

$$\left| V_{sys1} - V_{sys0} \right| = \left| \frac{p_{sys0}}{p_{sys1}} - 1 \right| V_{sys0} \quad (S5)$$

This value is proportional to the initial volume of the system V_{sys0} , and increases with the pressure change from the initial state. In our bi-shell valve, the maximum change in pressure from the initial state (atmosphere pressure $p_{sys0} = p_{atm} = 1.01 \times 10^5$ Pa) is below 550 Pa, which yields

$$\left| \frac{p_{sys0}}{p_{sys1}} - 1 \right| < 0.54\% \quad (S6)$$

We can thus rewrite the volume change due to air compressibility as

$$\frac{\left| V_{sys1} - V_{sys0} \right|}{V_{sys0}} < 0.54\% \quad (S7)$$

For our tests on the bi-shell valve, the total volume is about $V_{sys0} = 1.8 \times 10^5$ mm³, leading to a volume change of $\left| V_{sys1} - V_{sys0} \right| < 9.9 \times 10^2$ mm³. For the characterization of a separate shell, the total volume of the system is about $V_{sys0} = 5 \times 10^4$ mm³, leading to a volume change of

$|V_{sys1} - V_{sys0}| < 2.7 \times 10^2 \text{ mm}^3$. These values are tiny in comparison with the volume change of the shells ($\sim 1.3 \times 10^4 \text{ mm}^3$ for the bi-shell valve and $\sim 7.5 \times 10^3 \text{ mm}^3$ for a single shell), and corroborate the assumption made in this work that air compressibility can be neglected. Hence, the volume change of the syringe can be assumed as the volume change of the bi-shell valve and the separate shells.

S4. Finite element analysis

To further investigate the mechanical performance of the bi-shell valve, we conduct a set of finite element method (FEM) simulations with the commercial software package ABAQUS/STANDARD. The shell material is modelled as an incompressible neo-Hookean solid. The Young's modulus and Poisson's ratio (1.23 MPa and 0.5) are determined by fitting the simulation results with the experimental data within a range previously used in the literature.^[1, 3] This leads to the adoption of the following coefficients for our neo-Hookean model: $C10 = 0.205 \text{ MPa}$ and $D1 = 0 \text{ MPa}^{-1}$. We employ the modified Riks method to simultaneously solve for pressure and shell deformation. Since in our experiments we observe that both the imperfect shell and the spherical cap exhibit only an axisymmetric mode of deformation, we build our numerical model with axisymmetric elements (the two-node linear shell element SAX1 or the four-node bilinear quadrilateral element CAX4RH) to avoid the expensive computational cost of three-dimensional simulations. Although in some cases the imperfect shell may exhibit non-axisymmetric deformations, our previous study shows that an axisymmetric analysis can still be sufficient to retain a high level of accuracy.^[2] We impose a fixed boundary condition at the bottom of the shells and a uniform pressure at their surfaces. The volume change ΔV is calculated with the pressure p and the total external work done by the pressure U_p , which is given by

$$\Delta V = \int \frac{1}{p} dU_p. \quad (\text{S8})$$

As described below, our computational analysis for each separate shell as well as for the bi-shell valve is conducted into two steps. First, we consider an as-designed (ideal) model that is free from any manufacturing imperfections and does not account for any initial deformation caused by the clamping of the bottom ring. In this scenario, we systematically explore the geometric space of the bi-shell valve to unveil its sensitivity to a varying shell geometry. Second, to validate our numerical model with experimental results, we develop a set of realistic models, one for the spherical cap and the other for the imperfect shell. These models enable to capture the effect of the initial deformation due to clamping in spherical cap, and to incorporate as-manufactured imperfections, in particular thickness variations, in fabricated imperfect shells.

S4.1. Modelling of the spherical cap

As-designed model. The as-designed spherical cap is modelled with axisymmetric line element SAX1. The geometry of the spherical cap is $t_1/R = 0.05$, $h/R = 0.2$, and $R = 25$ mm. A mesh convergence study shows that 51 elements are sufficient to model the spherical cap (Figure S7A). In this work, around 51 elements are used for the spherical cap. To systematically study the response of the spherical cap with varying geometry, we explore the geometry space defined by the normalized thickness t_1/R ranging from 0.01 to 0.1 and the normalized height h/R spanning from 0.1 to 0.5; the radius at the base is fixed as $R = 25$ mm.

Realistic model. To capture cross-section variation in a representative sample of the spherical cap, we use a digital camera EOS 800D (Canon, Japan). Our observations show that the

spherical cap has a uniform thickness profile (Figure S8A), hence our analysis of the spherical cap studies only the role of the initial deformation due to clamping.

In Figure S9A, the spherical cap is modelled with CAX4RH elements, whereas the acrylic plate that clamps the base of the cap is modelled with rigid body line elements RAX1. For the spherical cap, our mesh convergence study shows that four elements through the thickness are sufficient (Figure S7B). Hence, we employ here at least four elements through the thickness.

The interaction between the cap and the plate is set as “hard” contact with a friction coefficient of 0.5. To investigate the effects of the initial deformation due to clamping, we first apply a downward displacement on the plate, and then apply a pressure on the shell to deflate the shell. The displacement is systematically varied from 0 (no clamping) to 0.3 mm (tight clamping). In Figure S9B, when the cap is clamped through the plate for 0.3 mm, an upward displacement occurs at the top of the cap. In Figure S10A, we find that the buckling pressure increases monotonically with the displacement of the clamping plate over a wide range of values from 403 Pa (no clamping) to 587 Pa (0.3 mm of clamping). From this set of results for the spherical cap, we decide to include the initial deformation due to clamping in our realistic numerical model. To minimize the difference of results between experiments and simulations, the displacement due to clamping is set as 0.1026 mm. This enables to yield a buckling pressure close to that of the representative sample of the spherical cap (Figure 2E), and to bring below 0.6% the relative error in the buckling pressure between simulation and experiment. In addition, we find that the buckling pressure of the unclamped case (Figure S10A) is slightly lower than the results in Figure S7. The reason for this is that in the simulations that study the effect of clamping, the thick band at the base of the shell is included; this provides an elastic support to the shell which is dissimilar to the fixed boundary condition employed in other simulations.

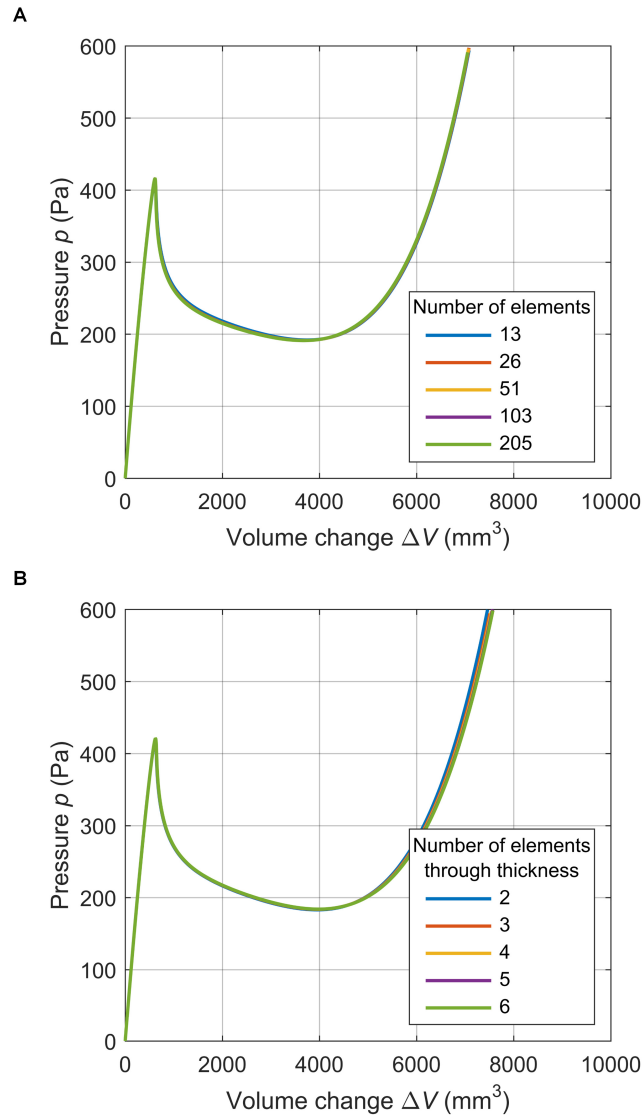


Figure S7. Mesh convergence study of the spherical cap. (A) SAX1 element. (B) CAX4RH element. Curves of different colors overlay, thereby showing that the simulation results for meshes with given number of elements have converged.

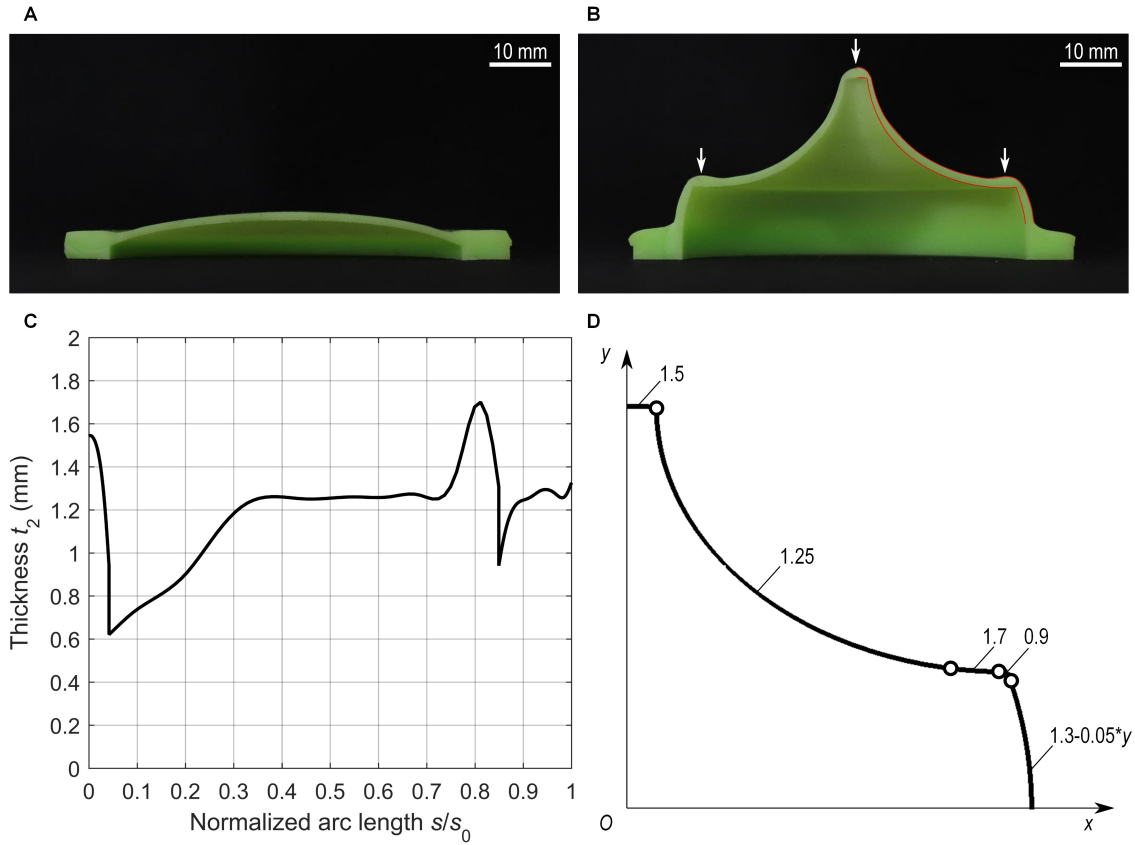


Figure S8. Cross-section of representative as-manufactured shell. (A) The spherical cap has a uniform thickness profile. (B) For the imperfect shell, on the other hand, the thickness profile is not uniform due to manufacturing. The red curves mark the upper and lower surfaces of half shell. The arrows marks the spots at the top of the shell and at the bottom of the imperfection with increased thickness. (C) Thickness t_2 of the imperfect shell measured as a function of the normalized arc length s/s_0 from the top ($s/s_0 = 0$) to the base ($s/s_0 = 1$). s and s_0 are the arc length and the total arc length. (D) Thickness profile of the imperfect shell used to generate the realistic computational model. The white dots partition the shell into five sections; to each of them the shell thickness is assigned separately to approximate the thickness distribution in (C). y is the distance from the base plane and the unit of the thickness is millimeter.

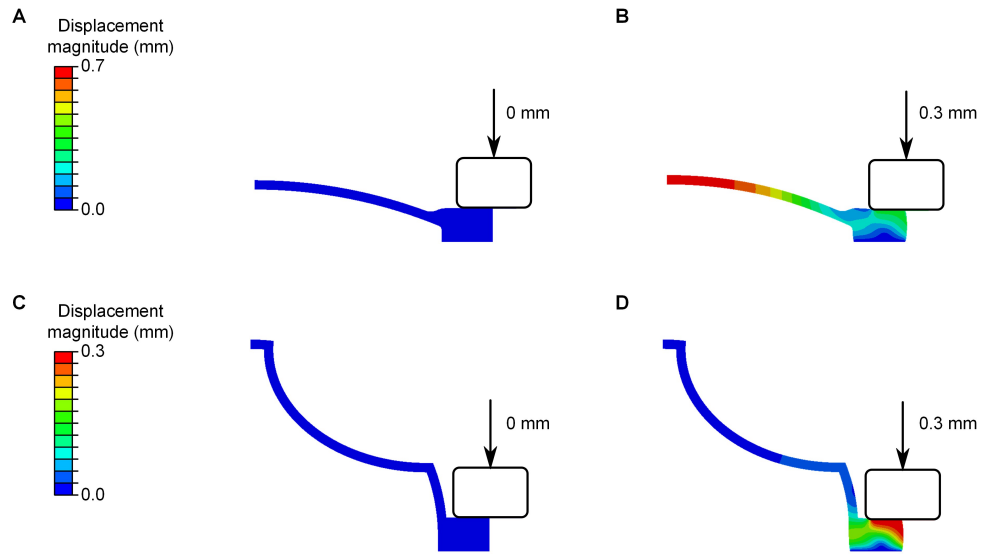


Figure S9. Deformation of the shells due to clamping. (A) Initial and (B) clamped configuration of the spherical cap. (C) Initial and (D) clamped configuration of the imperfect shell.

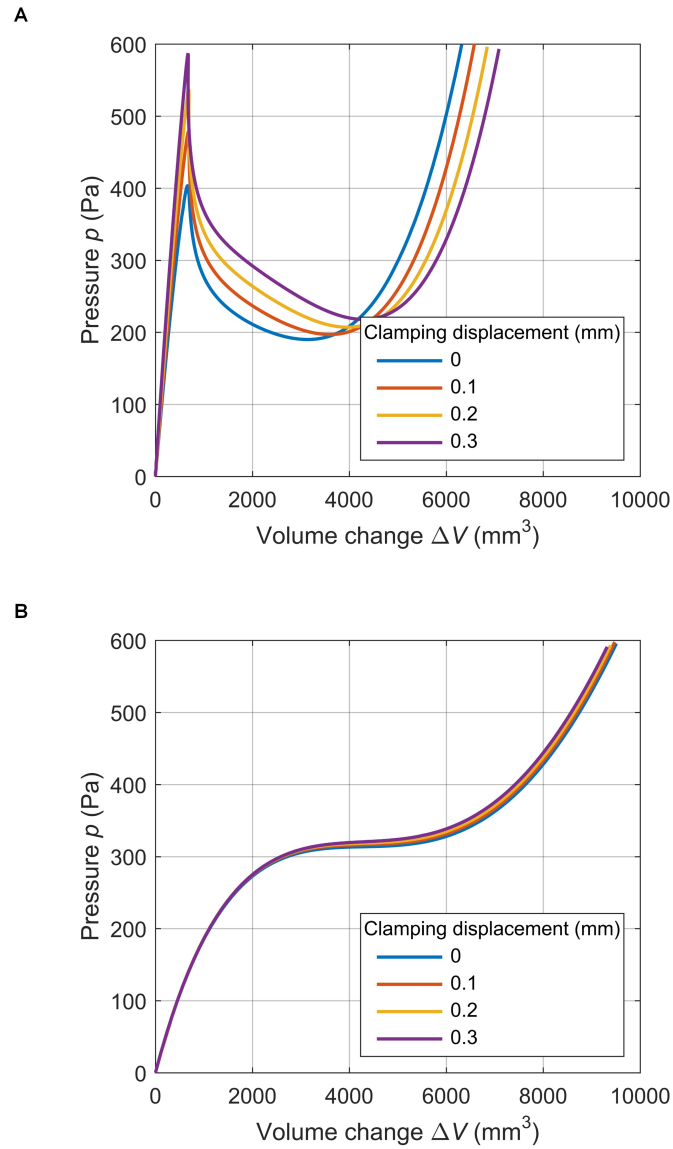


Figure S10. Pressure-volume responses of clamped shells. (A) spherical cap, and (B) imperfect shell.

S4.2. Modelling of the imperfect shell

As-designed model

We model the as-designed imperfect shell using the axisymmetric shell element SAX1. The geometry of the imperfect shell is defined by the following parameters: $t_2/R = 0.05$, $\theta_L = 20^\circ$, $\theta_U = 85.9^\circ$, and $R = 25$ mm. A wide design space is explored to investigate the

buckling sensitivity to the as-designed defect in the form of an ellipse, with respect to the normalized thickness ($0.02 \leq t_2/R \leq 0.1$) and meridional angle at the upper and lower boundary of the defect ($20^\circ \leq \theta_L \leq \theta_U \leq 85^\circ$). A mesh convergence study shows that 81 SAX1 elements are sufficient to model the imperfect shell (Figure S11A). In this work, an average of 81 elements are used for the imperfect shell.

Realistic model

As described above, our fabrication process, in particular the mould we used to produce our samples, had the following outcome on the shell geometries. The thickness profile of the spherical cap is uniform since the mould has no change in curvature, as opposed to that of the imperfect shell, which has variations due to abrupt changes in the curvature of the mould. To develop a realistic model of the imperfect shell with response that parallels that of the as-manufactured geometry, we investigate separately the role of non-uniform thickness as well as that of the initial deformation due to clamping, as described below.

Non-uniform thickness profile. Figure S8B shows that the as-manufactured shell features a thickness build up at locations above and below the elliptical arc; it is at those points that sudden changes of curvature appear in the mould. To obtain precise measurement of the thickness profile of the imperfect shell, we determine the distance between the inner and outer surfaces of the shell first from digital images (e.g. Figure S8B), and then by rectifying the data with measurements taken through a digital caliper (Figure S8C). This set of results is used to generate a numerical model that captures thickness variations along the shell profile; in particular the thickness profile of the shell is partitioned into five sections (Figure S8D), and to each of these portions the pertinent thickness is assigned. The SAX1 element is used to generate the model.

Initial deformation due to clamping. Here we solely study the role of the initial deformation due to clamping on an imperfect shell with uniform thickness. Figure S9C shows an imperfect

shell clamped to the fixture plate. The plate is modelled as a rigid body with the axisymmetric rigid two-node line element RAX1. Since the clamped base of the imperfect shell is too thick to be considered as a shell, we use the axisymmetric quadrilateral element CAX4RH instead of the SAX1 element. Our mesh convergence study shows that four elements through the thickness are sufficient for the imperfect shell (Figure S11). Hence, at least four elements through the thickness are adopted. The interaction between the shell and the clamp is set as “hard” contact with a friction coefficient of 0.5. In our simulations, we first simulate the initial deformation by imposing a vertical displacement on the plate, and then apply a pressure on the shell to deflate the shell. The displacement of the plate is varied from 0 to 0.3 mm. Figure S9D shows that the deformation due to clamping is localized at the base, while the body of the shell is not affected. In Figure S10B, the response of the imperfect shell is also not sensitive to the initial deformation caused by clamping. From these results, we conclude that it is reasonable to neglect the initial deformation of the imperfect shell due to clamping.

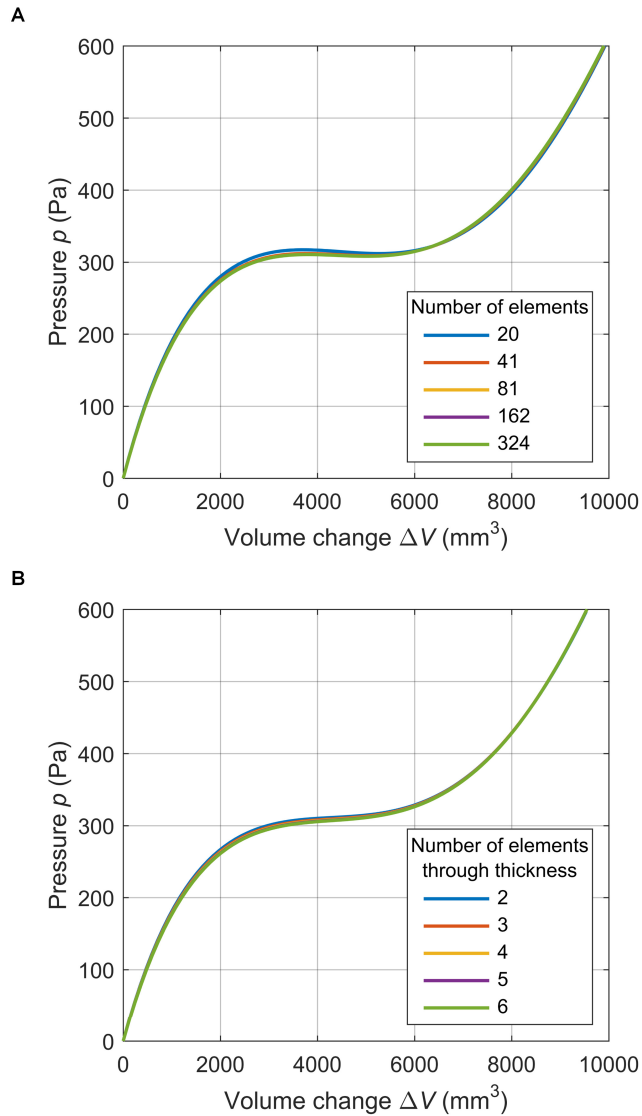


Figure S11. Mesh convergence study of the imperfect shell. (A) SAX1 element. (B) CAX4RH element. Curves of different colors overlay, thereby showing that the simulation results for meshes with given number of elements have converged.

S4.3. Modelling of the bi-shell valve

We now study the collective response of the shells forming our valve system by combining the models of each individual shell into one model. SAX1 elements are used for both constituent shells of the as-designed model, which does not feature any variation in thickness

or initial deformation due to clamping. On the other hand, for the realistic model, the thickness variation in the imperfect shell and the initial deformation of the spherical cap are modelled as described above for the realistic model of each shell.

We impose a uniform pressure on both shells, and trace the equilibrium path of the bi-shell system with the modified Riks method. The released energy is calculated as the negative of the area under the pressure-volume curve

$$\Delta U^* = -\int_S p dV \quad (\text{S9})$$

where S is the equilibrium path from the pre-snapping state (i) to the post-snapping state (ii) (Figure 1).

S5. Buckling modes of imperfect shell

While the buckling of the spherical cap subject to uniform pressure has been extensively studied in literature,^[1, 4, 5] only recently we unveil that of an imperfect shell with a large axisymmetric defect away from the pole.^[2] Therein, we investigated an individual imperfect shell with a circular defect, and demonstrated the existence of additional three buckling modes, besides to the classical bifurcation, that can be programmed on demand through geometry tuning.

In the current work, we amend the defect geometry to an elliptical arc for the convenience of manufacturing, and specify two defining parameters (Figure 4B): the meridional angles at the upper and lower boundary of the defect θ_U and θ_L . By varying θ_U and θ_L , we can show the emergence of four possible buckling modes (Figure S12). For a small defect (Figure S12A), the shell defect undergoes the classical bifurcation buckling, which is characterized by a downward dimple at the pole of the hemisphere. The pressure increases rapidly to a high buckling pressure (bifurcation point) before dropping immediately to a low plateau. We name this mode as mode 1.^[2] When the defect size increases, Figure S12B shows that the buckling

mode changes from the classical bifurcation mode to a snap-through buckling mode, which is characterized by a localized deformation that evolves mainly within the defect (mode 2). Similar to mode 1, the pressure attains the maximum at a small volume change (limit point 1). For further increase of defect size (Figure S12C), the maximum pressure is reached when the main deformation localizes below the defect (mode 3). Dissimilar from mode 1 and mode 2, the pressure in mode 3 gradually increases to the maximum at a much larger volume change (limit point 2). Depending on the shell geometry, the pressure may also show a plateau before the attainment of the maximum pressure (Figure 1E). In a special case (Figure S12D), the shell buckles with a mixed mode that combines mode 2 and mode 3. The pressure shows a lower peak at a small volume change (limit point 1) before finally attaining the maximum value at a large change in volume (limit point 2).

The four buckling modes identified above can be overlaid onto the map of the attainable valve output illustrated in Figure 4. The result is shown in Figure S13. Here, the boundary (red line) is marked between mode 1 and 2, where the imperfect shell collapse immediately upon deflation, and the zone of mode 3 and 4, where the imperfect shell can undergo a large deformation before collapse. The region of mode 1 and 2 is on the lower right-hand side of the red line where θ_U and θ_L are close in value (small defect), whereas the zone of mode 3 and 4 is on the other side where the defect is large.

The map in Figure S13 helps gain essential insights into the role the shell defect plays on the performance of our bi-shell valve. In particular, the domain boundaries demonstrate that to maximize the valve output, values of θ_U and θ_L falling within the zone of mode 3 and 4 should be preferred, as opposed to those of the other zone (mode 1 and 2), where the valve output is practically null. The cause for the difference we observe here lies in the interaction between the spherical cap and the imperfect shell, as discussed in Section S6 of Supporting Information.

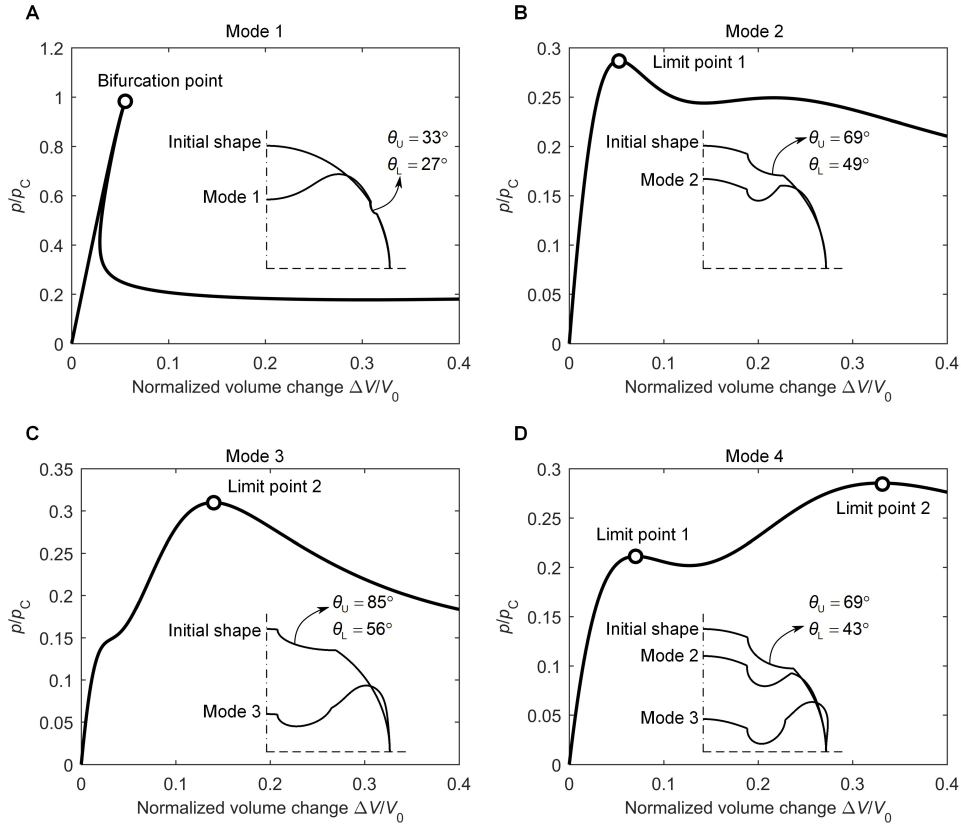


Figure S12. Possible deformation modes leading to shell collapse. (A) Mode 1: Bifurcation buckling with a dimple-like shape response. (B) Mode 2: Snap-through buckling 1 characterized by localized deformation within the imperfection. (C) Mode 3: Snap-through buckling 2 with localized deformation below the imperfection. (D) Mode 4: Snap-through buckling combining mode 2 and 3.

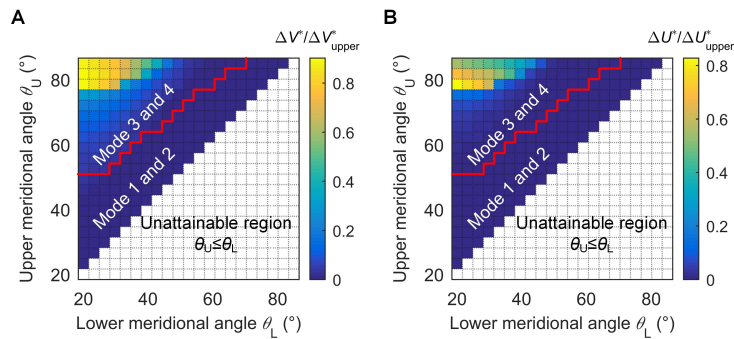


Figure S13. Attainable valve output with corresponding buckling modes. (A) Attainable volume change. (B) Attainable released energy. The red line marks the boundary between the zone of mode 1 and 2 and the zone of mode 3 and 4.

S6. Interaction between spherical cap and imperfect shell

S6.1. Interaction between shells

In our bi-shell valve, the total volume change of the imperfect shell and the spherical cap is determined by the input volume change dispense by the syringe. Since the air compressibility can be neglected (see S3), the sum of the volume change of each shell (ΔV_1 and ΔV_2) should balance that of the syringe (ΔV_{in}) such that

$$\Delta V_1 + \Delta V_2 = \Delta V_{in} \quad (\text{S10})$$

When the imperfect shell and the spherical cap are slowly deflated by the syringe, their pressure at the quasi-equilibrium state must be equal

$$p_1(\Delta V_1) = p_2(\Delta V_2) \quad (\text{S11})$$

where $p_1(\Delta V_1)$ and $p_2(\Delta V_2)$ are the pressure of each shell as a function of its own volume change. Substituting Equation S10 into Equation S11 yields

$$p_1(\Delta V_1) = p_2(\Delta V_{in} - \Delta V_1) \quad (\text{S12})$$

At the pre-snapping state (i), Equation S11 and S12 are rewritten as

$$p_1(\Delta V_{1(i)}) = p_2(\Delta V_{in(i)} - \Delta V_{1(i)}) = p_2(\Delta V_{2(i)}) \quad (\text{S13})$$

where the subscript (i) denotes the pre-snapping state. While the pre-snapping state of the spherical cap is determined by its own buckling point, the pre-snapping state of the imperfect shell can be determined by finding the value of $\Delta V_{2(i)}$ that satisfies Equation S13.

At the post-snapping state (ii), the balance of pressure is rewritten as

$$p_1(\Delta V_{1(i)} + \Delta V^*) = p_2(\Delta V_{in(i)} - (\Delta V_{1(i)} + \Delta V^*)) = p_2(\Delta V_{2(i)} - \Delta V^*) \quad (\text{S14})$$

where ΔV^* is the volume change due to snapping. Since $\Delta V_{1(i)}$ and $\Delta V_{2(i)}$ are already known from Equation S13, the post-snapping state (ii) can be determined by finding the volume change ΔV^* that satisfies Equation S14.

When the pre and post-snapping states have been determined, the released energy can be calculated from the separate response of each shell as

$$\Delta U^* = -\int_{\Delta V_{1(i)}}^{\Delta V_{1(ii)}} p_1 dV - \int_{\Delta V_{2(i)}}^{\Delta V_{2(ii)}} p_2 dV \quad (\text{S15})$$

where $\Delta V_{1(ii)} = \Delta V_{1(i)} + \Delta V^*$ and $\Delta V_{2(ii)} = \Delta V_{2(i)} - \Delta V^*$ are the volume changes at the post-snapping states.

Since Equation S15 does not require handling the simulation of the whole valve, rather it allows to determine the global performance of the valve from those of the constituents. For this reason, the approach that we propose in this work enables a sizeable reduction of the computational cost, and can be readily used to compute the attainable valve output that is plotted in Figure 4.

S6.2. Relation between shell interaction and valve output

Equation S10 to S15 provide a mathematical description of the general interaction between the shells. However, they have been applied neither to assess the pressure volume curves of the individual shells nor to calculate the valve output. In this section, we apply these equations to analyze a group of pressure-volume curves with changing thickness so as to further explain the relation between shell interaction and valve output. Our specific focus is on understanding the reason for the small yellow regions in Figure 4, where the volume change and released energy reach the maximum values.

Figure S13 shows a set of the pressure-volume responses of the shells illustrated in Figure 4B. The curves pertain to a spherical cap (red line) and an array of imperfect shells with varying thickness t_2/R (green and black lines). A range of responses can be observed.

- The green curves represent imperfect shells with $0.045 < t_2 / R < 0.055$. Here, the plateau pressure is located between the pre and post-snapping pressure p_i and p_{ii} , thereby allowing a large volume change at the plateau stage attained with a minor decrease in pressure resistance. This large volume change is a prerequisite for the shell to release a large amount of energy, hence to maximize the valve performance output. When the plateau pressure values gradually approaches p_i with increasing thickness t_2 / R , the released energy reaches a maximum value of $\Delta U / \Delta U_{\text{upper}} = 0.70$ at $t_2 / R = 0.054$ with a sizeable volume change of $\Delta V / \Delta V_{\text{upper}} = 0.81$.
- On the other hand, the black lines describe responses governed by $t_2 / R < 0.045$ and $t_2 / R > 0.055$. In this case, the plateau pressure is either lower or higher than both the pre and post-snapping pressure. Snapping occurs outside the plateau stage, thus causing a fast drop in pressure from p_i to p_{ii} . This set of imperfect shells (black) can only snap for a tiny volume change, and release a small amount of elastic energy as opposed to the imperfect shells in the range $0.045 < t_2 / R < 0.055$. Moreover, the thinnest shell with $t_2 / R = 0.02$ have a maximum pressure that is lower than the buckling pressure of the spherical cap. In this case, the bi-shell system cannot snap because the pressure is unable to reach the buckling pressure of the cap.

A comparison of Figure S12 with Figure S14 highlights that only mode 3 and 4 are suitable for the bi-shell valve. In mode 1 and 2, the pressure of the imperfect shell quickly reaches the maximum with a small volume change. On one hand, if the maximum pressure is larger than the buckling pressure of the spherical cap, the shell interaction will be similar to the case in Figure S14 for thick imperfect shells with $t_2 / R > 0.055$ (black lines on the left). The bi-shell valve can only snap for a small volume change and released energy. On the other hand, if the maximum pressure is less than the buckling pressure of the spherical cap, there will be no

snapping at all, as in the case with the thinnest imperfect shell ($t_2/R = 0.02$). In mode 3 and 4, the imperfect shell can undergo a large deformation before attaining the maximum pressure, a response that can potentially form a plateau of pressure before collapse. The green lines in Figure S14 therefore identify the set of bi-shell valves that can attain a large volume change when the plateau pressure is between the pre and post-snapping states; in addition, their maximum values of released energy can be obtained when the plateau pressure is just below the pre-snapping pressure.

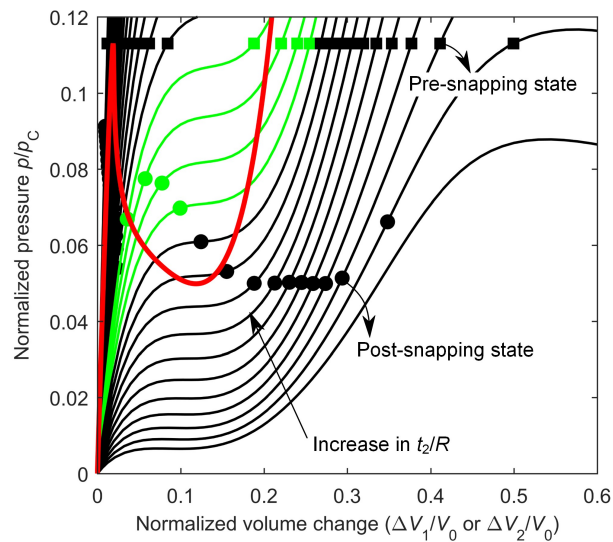


Figure S14. Pressure-volume response of the shells in Figure 4B. The red curve represents the spherical cap. The green lines describe imperfect shells in the range of $0.045 < t_2/R < 0.055$, while the black curves pertain to the remaining set of imperfect shells ($0.02 \leq t_2/R < 0.045$ and $0.055 < t_2/R \leq 0.1$). The square and circular dots mark the pre and post-snapping states of each imperfect shell.

S7. Upper bounds of valve output

Here we study the upper bounds of our valve output for both volume and released energy.

Figure S15 shows two representative curves of pressure-volume, each representing one individual shell, the spherical cap (A) and the imperfect shell (B). Upon snapping, the

pressure of both shells decreases from p_i to p_{ii} . In ideal conditions, we could assume the post-snapping pressure of the imperfect shell retains the pre-snapping pressure p_i (dashed line in Figure S15B). Thus, the pressure of the spherical cap could also retain p_i , thus leading to a post-snapping volume change of $\Delta V_{1(iii)}$ (Figure S15A). Since it is unrealistic for the imperfect shell to have a post-snapping pressure higher than p_i , the post-snapping volume change of the spherical cap will never get larger than $\Delta V_{1(iii)}$. Thus, $\Delta V_{\text{upper}}^* = \Delta V_{1(iii)} - \Delta V_{1(i)}$ is the upper bound for the volume change output.

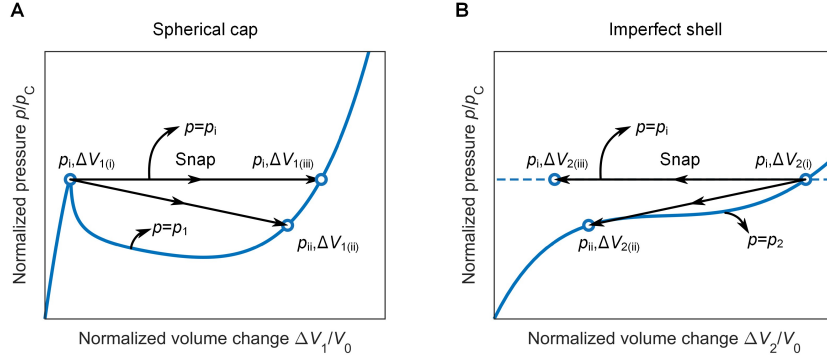


Figure S15. Representative pressure-volume responses of individual shells. (A) Spherical cap. (B) Imperfect shell. The dashed line in (B) shows an ideal scenario describing the case where the pressure of the imperfect shell does not drop after snapping; this phenomenon leads to state (iii) with pressure p_i and volume change $\Delta V_{2(iii)}$.

As per the released energy, we can use Equation S15 to rewrite the energy released from state (i) to (ii)

$$\begin{aligned}
\Delta U_{(ii)}^* &= -\int_{\Delta V_{1(i)}}^{\Delta V_{1(ii)}} p_1 dV - \int_{\Delta V_{2(i)}}^{\Delta V_{2(ii)}} p_2 dV \\
&= -\int_{\Delta V_{1(i)}}^{\Delta V_{1(iii)}} p_1 dV - \int_{\Delta V_{1(ii)}}^{\Delta V_{1(iii)}} p_1 dV - \int_{\Delta V_{2(i)}}^{\Delta V_{2(ii)}} p_2 dV - \int_{\Delta V_{2(ii)}}^{\Delta V_{2(iii)}} p_1 dV + \int_{\Delta V_{2(ii)}}^{\Delta V_{2(iii)}} p_i dV \\
&= \left(-\int_{\Delta V_{1(i)}}^{\Delta V_{1(iii)}} p_1 dV - \int_{\Delta V_{2(i)}}^{\Delta V_{2(iii)}} p_i dV \right) + \left(-\int_{\Delta V_{1(ii)}}^{\Delta V_{1(iii)}} p_1 dV - \int_{\Delta V_{2(i)}}^{\Delta V_{2(ii)}} p_2 dV + \int_{\Delta V_{2(ii)}}^{\Delta V_{2(iii)}} p_i dV \right) \quad (\text{S16}) \\
&= \Delta U_{(iii)}^* + \left(\int_{\Delta V_{2(i)}}^{\Delta V_{2(iii)}} p_i dV - \int_{\Delta V_{1(ii)}}^{\Delta V_{1(iii)}} p_1 dV + \int_{\Delta V_{2(ii)}}^{\Delta V_{2(iii)}} p_i dV - \int_{\Delta V_{2(i)}}^{\Delta V_{2(ii)}} p_2 dV \right)
\end{aligned}$$

where $\Delta U_{(ii)}^*$ is the released energy from state (i) to (ii), $\Delta U_{(iii)}^*$ is the released energy from state (i) to (iii). Here the snapping pressure of the spherical cap p_i is a constant, while p_1 and p_2 are function of the volume change of each shells (blue lines in Figure S15).

Since the total volume change is constant during snapping, according to Equation S10 we have

$$\Delta V_{1(i)} + \Delta V_{2(i)} = \Delta V_{1(ii)} + \Delta V_{2(ii)} = \Delta V_{1(iii)} + \Delta V_{2(iii)} \quad (\text{S17})$$

The first two terms in the bracket of the last row of Equation S16 are

$$\begin{aligned} \int_{\Delta V_{2(ii)}}^{\Delta V_{2(iii)}} p_1 dV - \int_{\Delta V_{1(ii)}}^{\Delta V_{1(iii)}} p_1 dV &= p_i (\Delta V_{2(iii)} - \Delta V_{2(ii)}) - \int_{\Delta V_{1(ii)}}^{\Delta V_{1(iii)}} p_1 dV \\ &= p_i (\Delta V_{1(ii)} - \Delta V_{1(iii)}) - \int_{\Delta V_{1(ii)}}^{\Delta V_{1(iii)}} p_1 dV \\ &= \int_{\Delta V_{1(ii)}}^{\Delta V_{1(iii)}} p_i dV - \int_{\Delta V_{1(ii)}}^{\Delta V_{1(iii)}} p_1 dV \end{aligned} \quad (\text{S18})$$

Since $\Delta V_{1(ii)} < \Delta V_{1(iii)}$ and $p_i \geq p_1$, we have

$$\int_{\Delta V_{2(ii)}}^{\Delta V_{2(iii)}} p_i dV - \int_{\Delta V_{1(ii)}}^{\Delta V_{1(iii)}} p_1 dV = \int_{\Delta V_{1(ii)}}^{\Delta V_{1(iii)}} p_i dV - \int_{\Delta V_{1(ii)}}^{\Delta V_{1(iii)}} p_1 dV < 0 \quad (\text{S19})$$

Similarly since $\Delta V_{2(i)} > \Delta V_{2(ii)}$ and $p_i \geq p_2$, the last two terms in the bracket of the last row of Equation S16 satisfies

$$\int_{\Delta V_{2(ii)}}^{\Delta V_{2(i)}} p_1 dV - \int_{\Delta V_{2(ii)}}^{\Delta V_{2(i)}} p_2 dV < 0 \quad (\text{S20})$$

Finally, Substituting Equation S19 and S20 into S16, we have

$$\Delta U_{(ii)}^* < \Delta U_{(iii)}^* \quad (\text{S21})$$

The above demonstrate that $\Delta U_{\text{upper}}^* = \Delta U_{(iii)}^*$ is the upper bound of the released energy. State (iii) therefore describe the upper bounds of both volume change and released energy, which are theoretical limits fully determined by the spherical shell. The volume change and released

energy output of a given bi-shell valve can never surpass them, because the inflation of the imperfect shell during snapping can only cause a decrease in pressure.

S8. Flow chart of the design process

Figure S16 shows the two-steps approach here proposed for the design of our bi-shell valve. It involves the 4 metrics introduced in the main text of the paper: the upper bounds of volume and energy ($\Delta V_{\text{upper}}^*$ and $\Delta U_{\text{upper}}^*$) and the attainable ranges of output (ΔV^* and ΔU^*) within their respective bounds.

The focus of the first step is on the spherical cap only, and aims at identifying the upper bounds ($\Delta V_{\text{upper}}^*$ and $\Delta U_{\text{upper}}^*$) of the valve output. These quantities set the performance limits imposed by the spherical cap to a bi-shell system with any geometric parameters of the imperfect shell. With these upper bounds, we can select the geometry of a spherical cap (t_1/R and h/R) that meet the requirements of volume and energy output prescribed by a given application.

In the second step, the emphasis shifts to the imperfect shell, and the goal is to obtain the attainable ranges of volume change ΔV^* and released energy ΔU^* for a bi-shell valve with the spherical cap selected in the first step. We do so by first exploring the design space of the imperfect shell. Then, we complete the valve design by selecting a set of the imperfect shell parameters, i.e. t_2/R , θ_U and θ_L , that can meet the valve output requirements of the application (ΔV^* and ΔU^*). If there is no feasible design for the imperfect shell, we then return to the first step to revise the design of the spherical cap. With this approach, we can ensure to fully tap into the full potential of both shells and obtain a valve output that is close to the achievable maximum.

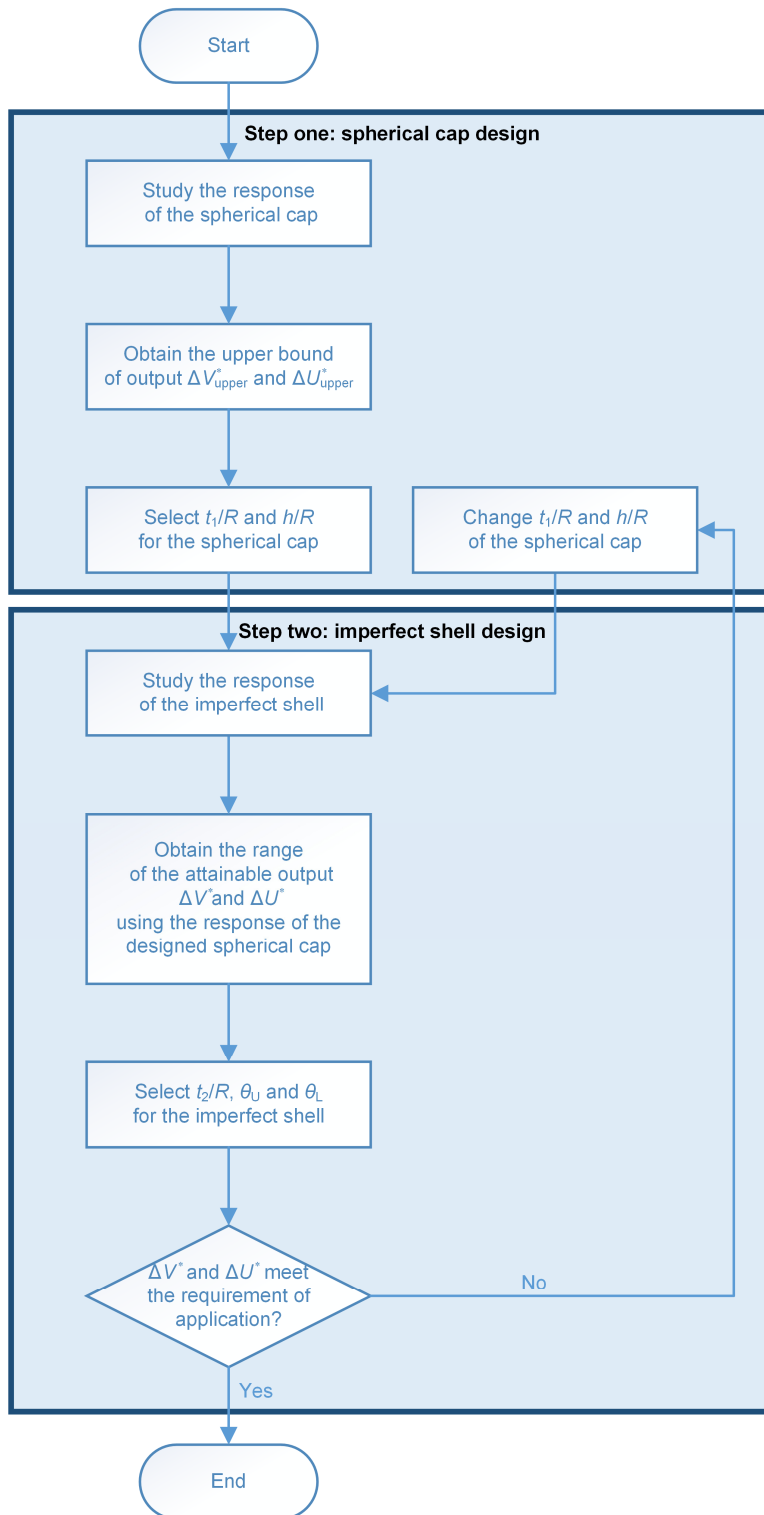


Figure S16. Design flowchart describing the steps to design the bi-shell valve.

S9. Alternative designs of the bi-shell valve

The bi-shell valve introduced in the main text operates through deflation. Here we introduce two design variations to achieve alternative functions: a *pneumatic volume fuse* and a *rapid inflation valve*.

- Figure S17A shows a *pneumatic volume fuse*. This concept modifies the original bi-shell valve operating in a deflation mode in the position of the output chamber, which is here moved on the top of the imperfect shell. In this configuration, before snapping, the imperfect shell can be deflated to generate a continuous volume output ΔV_2 (Figure S17B). When the imperfect shell is in the pre-snapping state (i), further deflation will trigger the snapping of the volume fuse, which reduces the volume change of the imperfect shell from state (i) to state (ii). The outcome is a pneumatic fuse: the volume change of the imperfect shell at state (i) sets the threshold of volume output that the fuse cannot exceed.
- Figure S17C shows a *rapid inflation valve*. The original bi-shell valve concept is here altered by flipping the two elastic shells upside down. This valve works in inflation mode in a way similar to that of the original valve that operation in a deflation mode. When slowly inflated at the inlet (Figure S17D), the imperfect shell first inflates to store energy and volume change. Upon snapping, the imperfect shell deflates from state (i) to state (ii) so as to release energy and volume change, while the spherical cap snaps upward. The advantage of this design is the provision of a fast volume output for the rapid inflation of any actuator that may be connected to the outlet.

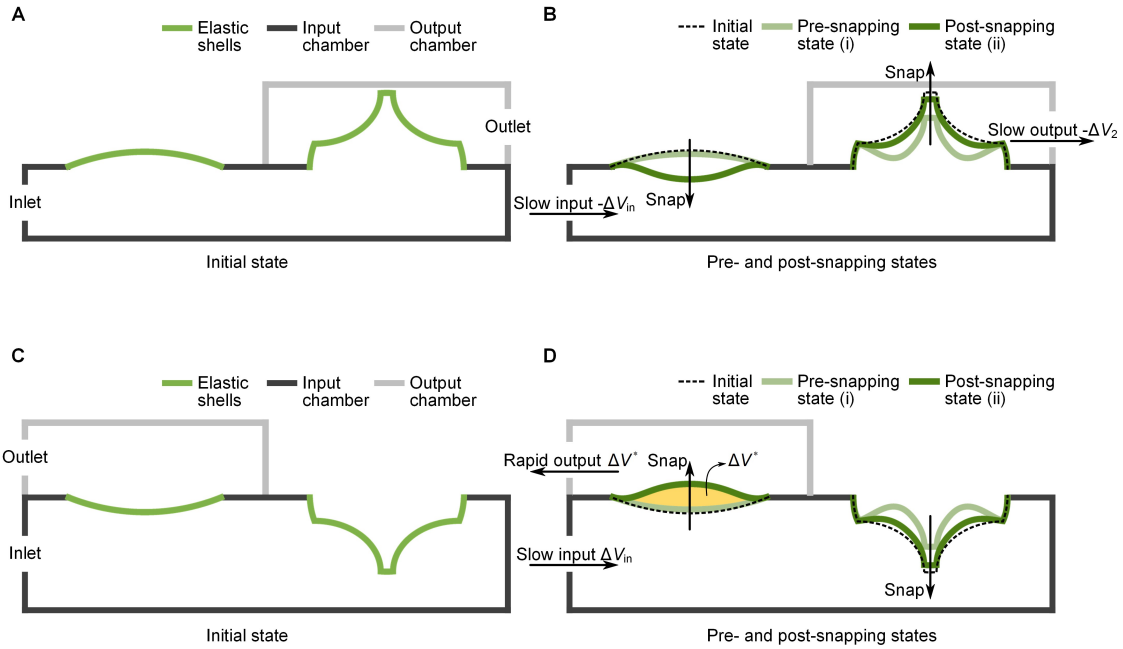


Figure S17. Alternative valve designs. (A) and (B) pneumatic volume fuse. (C) and (D) rapid inflation valve.

S10. Effect of elastic modulus on the performance of the bi-shell valve

To study the effect of material elasticity on the performance of the bi-shell valve, we perform a set of numerical simulations, where the shell material is assumed linear elastic with a Young's modulus ranging between 1 and 10 MPa. The geometry of the spherical cap and the imperfect shell are defined as: $R = 25 \text{ mm}$, $t_1 / R = t_2 / R = 0.05$, $h / R = 0.2$, $\theta_l = 20^\circ$, and $\theta_U = 85.9^\circ$.

In Figure S18A, the pressure increases linearly with the Young's modulus, while the volume change is not affected by a change in the Young's modulus values. In Figure S18B, the released energy of the bi-shell valve increases linearly with the Young's modulus from 1 to 10 MPa with discrete step of 1 MPa. On the other hand, the volume output of the valve is not affected by a change in the Young's modulus values (Figure S18C).

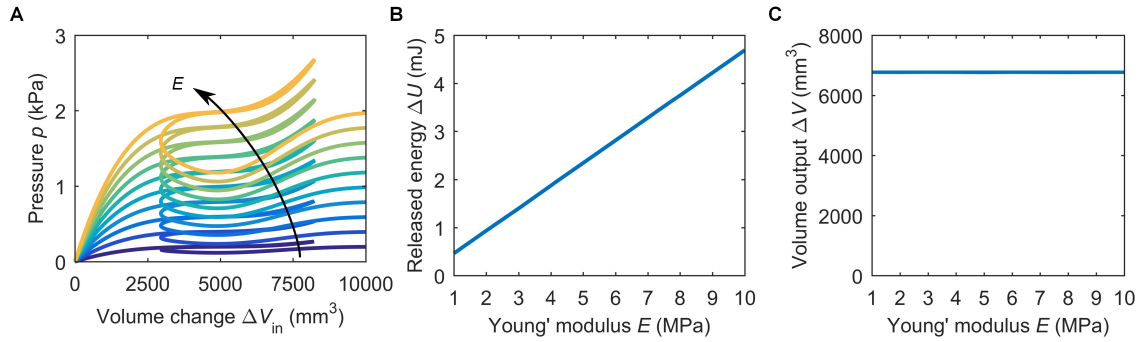


Figure S18. Influence of elastic modulus. (A) Pressure-volume change curves, (B) released energy ΔU , and (C) volume output ΔV of bi-shell valves with Young's modulus E increasing from 1 to 10 MPa with discrete step of 1 MPa.

S11. Integration of the bi-shell valve integrated into a soft robot or actuator.

To integrate our valve within a soft robot, the output chamber can be merged with the interior of the soft actuator, while the whole system of the bi-shell valve and the soft actuator can be controlled from the input chamber. A possible layout of the valve-actuator integration is given in Figure S19. Both the rigid input and output chambers can be replaced with thick soft walls by molding^[6]. The integration would only require the merging of both molds, that of the bi-shell valve and that of the soft actuator. The exterior of the robot is purposely left as undefined because it can be shaped by design to deliver a certain function. For example to achieve motion, the exterior body can be designed as a partially corrugated cylinder with grips in contact with the ground.^[6]

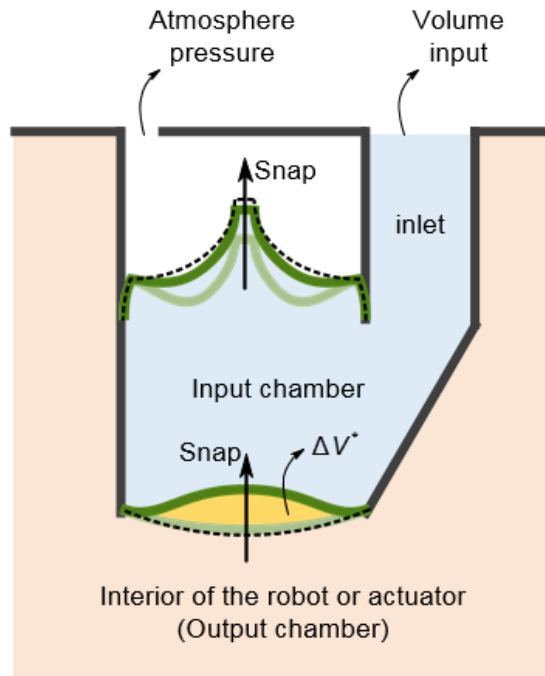


Figure S19. Schematic of the bi-shell valve integrated into a soft robot or actuator.

S12. Scenario of a similar valve with only one shell

If there is only the spherical cap (Figure S20), there can be no fast transfer of air volume between shells. This means that the total volume of the input and output chambers remains constant. As a result, the flow rate provided at the valve input equals that of the valve output. In our experiment, the flow rate at the valve inlet is 3 mL/min, a value that cannot provide fast actuation. On the other hand, if only the imperfect shell is present, fast actuation cannot yet be achieved. The reason is as for the above. No fast transfer of air volume between shells can occur, hence we cannot convert a low flow rate (input) to a fast flow rate (output).

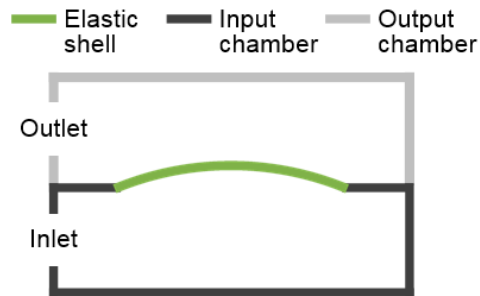


Figure S20. Scenario with only the spherical cap.

References

- [1] A. Lee, F. López Jiménez, J. Marthelot, J. W. Hutchinson, P. M. Reis, *J. Appl. Mech.-Trans. ASME* **2016**, 83, 111005.
- [2] C. Qiao, L. Liu, D. Pasini, *J. Mech. Phys. Solids* **2020**, 141, 103959.
- [3] M. Pezzulla, S. A. Shillig, P. Nardinocchi, D. P. Holmes, *Soft Matter* **2015**, 11, 5812.
- [4] J. W. Hutchinson, *Proc. R. Soc. A-Math. Phys. Eng. Sci.* **2016**, 472, 20160577.
- [5] J. Paulose, D. R. Nelson, *Soft Matter* **2013**, 9, 8227.
- [6] P. Rothmund, A. Ainla, L. Belding, D. J. Preston, S. Kurihara, Z. Suo, G. M. Whitesides, *Sci. Robot.* **2018**, 3, 7986.

Movie. S1. Snapping of the bi-shell valve.

Movie. S2. Fast pushing a table tennis ball with a striker actuated through the bi-shell valve.

Movie. S3. Actuation of the striker through the bi-shell valve.

Movie. S4. Actuation of the striker without the bi-shell valve.

Movie. S5. Reversible snapping of the bi-shell valve.